

# Petrology and Sr–Nd Isotopic Disequilibrium of the Xiaohaizi Intrusion, NW China: Genesis of Layered Intrusions in the Tarim Large Igneous Province

XUN WEI<sup>1,2,3</sup>, YI-GANG XU<sup>1\*</sup>, CHUAN-LIN ZHANG<sup>4</sup>, JIAN-XIN ZHAO<sup>5</sup>  
AND YUE-XING FENG<sup>5</sup>

<sup>1</sup>STATE KEY LABORATORY OF ISOTOPE GEOCHEMISTRY, GUANGZHOU INSTITUTE OF GEOCHEMISTRY, CHINESE ACADEMY OF SCIENCES, GUANGZHOU 510640, PR CHINA

<sup>2</sup>KEY LABORATORY OF MARINE GEOLOGY AND ENVIRONMENT, INSTITUTE OF OCEANOLOGY, CHINESE ACADEMY OF SCIENCES, QINGDAO 266071, PR CHINA

<sup>3</sup>UNIVERSITY OF CHINESE ACADEMY OF SCIENCES, BEIJING 100049, PR CHINA

<sup>4</sup>NANJING INSTITUTE OF GEOLOGY AND MINERAL RESOURCES, CGS, NANJING 210016, PR CHINA

<sup>5</sup>RADIOGENIC ISOTOPE FACILITY, SCHOOL OF EARTH SCIENCES, THE UNIVERSITY OF QUEENSLAND, BRISBANE, QLD 4072, AUSTRALIA

RECEIVED FEBRUARY 25, 2014; ACCEPTED NOVEMBER 14, 2014

*Layered mafic intrusions (LMI) are sporadically distributed in the Early Permian Tarim large igneous province (LIP), NW China, and are crosscut by numerous contemporaneous dykes. The Xiaohaizi wehrlite intrusion is composed mainly of olivine (Fo69–75), clinopyroxene (Mg# = 75–84), intercumulus plagioclase (An53–86) and Fe–Ti oxides. Both petrography and mineral compositions suggest that olivine and clinopyroxene crystallized earlier than plagioclase and Fe–Ti oxides. The dykes are of alkali basalt to trachyandesite with low Mg# (35–39). The least-contaminated dykes display strong rare earth element (REE) fractionation, enrichment of Nb and Ta, and depletion of Pb relative to other similarly incompatible elements, bearing strong similarity to ocean island basalts (OIB). This, together with their positive  $\epsilon Nd_i$  values (4.3–4.8), is consistent with derivation from an enriched asthenospheric mantle source. Clinopyroxenes in the wehrlites display convex-upward chondrite-normalized REE patterns. The melts in equilibrium with these clinopyroxenes have very similar trace element compositions to those of the crosscutting dykes, suggesting a similar mantle source shared by the Xiaohaizi wehrlite intrusion*

*and dykes. The Xiaohaizi wehrlite intrusion is characterized by Sr–Nd isotopic disequilibrium between clinopyroxene and plagioclase separates:  $^{87}Sr/^{86}Sr_i$  (0.7038–0.7041) and  $\epsilon Nd_i$  (1.0–1.9) of clinopyroxene are lower and higher than the respective ratios of intercumulus plagioclase ( $^{87}Sr/^{86}Sr_i$  = 0.7042–0.7043,  $\epsilon Nd_i$  = 0.4–1.0). The  $^{87}Sr/^{86}Sr_i$  and  $\epsilon Nd_i$  of clinopyroxene separates correlate positively and negatively with  $Zr/Nb$ , respectively, implying variable degrees of crustal contamination during the formation of the Xiaohaizi wehrlite intrusion.  $^{87}Sr/^{86}Sr_i$  increases and  $\epsilon Nd_i$  decreases with increasing Ca content of plagioclase, indicating that higher An plagioclases experienced higher degrees of contamination. This can be explained by assimilation of continental crust through a turbulent magma ascent (ATA) process. However, this ATA model fails to account for the positive correlation between the Mg# and  $\epsilon Nd_i$  of clinopyroxene separates. The isotopic disequilibrium in the Xiaohaizi LMI is more probably generated during an assimilation and fractional crystallization process involving Archean–Neoproterozoic basement and carbonates as contaminants.*

\*Corresponding author. Telephone: +86 20 85290109. Fax: +86 20 85290130. E-mail: yigangxu@gig.ac.cn

KEY WORDS: *Xiaohaizi intrusion; isotopic disequilibrium; assimilation and fractional crystallization; layered mafic intrusions; Tarim LIP*

## INTRODUCTION

Layered mafic intrusions (LMI) have been intensively studied for their unique trace element enrichment [e.g. PGE (platinum group elements), Cr, Ni, V, Ti], notably the Noril'sk–Talnakh Ni–Cu–PGE deposits in the Siberian Traps (Lightfoot *et al.*, 1990; Naldrett *et al.*, 1992; Hawkesworth *et al.*, 1995) and the Panzhihua and Hongge V–Ti–magnetite deposits in the Emeishan large igneous province (LIP) (Zhou *et al.*, 2005; Pang *et al.*, 2008b; Bai *et al.*, 2012; Song *et al.*, 2013). Their typical intra-cratonic setting makes them important for studying the evolution of cratonic domains and the role of crust–mantle interaction in their genesis (DePaolo & Wasserburg, 1979; Kruger *et al.*, 1987; Zhou *et al.*, 2005; Cawthorn, 2007; Day *et al.*, 2008; Richardson & Shirey, 2008; O'Driscoll *et al.*, 2009; Wilson, 2012; Nebel *et al.*, 2013). Most LMI formed via multiple magma injections into crustal magma chambers (Cawthorn *et al.*, 1991; Tegner *et al.*, 2006; Pang *et al.*, 2009; Namur *et al.*, 2010). The parental magmas of LMI have inevitably, to some extent, interacted with subcontinental lithospheric mantle (SCLM) and crust during ascent and emplacement (Maier *et al.*, 2000; Prevec *et al.*, 2005; Richardson & Shirey, 2008; Fourie & Harris, 2011; Roelofse & Ashwal, 2012). In this regard, crustal assimilation–fractional crystallization (AFC) processes may have played an important role in the magmatic evolution and petrogenesis of LMI. Prominent examples of AFC processes during the formation of LMI are the existence of isotopic disequilibrium within a single mineral or amongst coexisting minerals of cumulus rocks (Tepley & Davidson, 2003; Prevec *et al.*, 2005).

Study of the isotopic compositions of minerals, especially those crystallized during different stages of magmatic evolution from a common parental magma, may also shed light on the role of AFC processes in the generation of LMI. The Xiaohaizi LMI in the Early Permian Tarim LIP of NW China is composed of ~750 m of cumulate wehrlite consisting mainly of cumulus olivine and clinopyroxene with interstitial plagioclase and Fe–Ti oxides. Clinopyroxene and plagioclase in the Xiaohaizi intrusion represent the crystallized products at different stages of magmatic evolution; thus a careful study of mineral and Sr–Nd isotope compositions should provide insights into the role of the AFC process in the generation of LMI. In addition, the Xiaohaizi LMI is closely associated with syenites and crosscut by numerous contemporaneous mafic dykes. This also provides a good opportunity to investigate the magma plumbing system below an LIP.

LMI often host economic Fe–Ti oxide deposits; for example, the Panzhihua intrusion in the Emeishan LIP (Zhou *et al.*, 2005; Pang *et al.*, 2008b). In the Tarim LIP, V–Ti–magnetite mineralization is associated with the Wajilitag LMI, which is close to the Xiaohaizi intrusion (Zhang *et al.*, 2008a; Li *et al.*, 2012a; Cao *et al.*, 2014). Strong negative aeromagnetic anomalies also make the Xiaohaizi area a potential target for Fe–Ti oxide deposits. Fe–Ti oxide mineralization in LMI may be controlled by the composition of the parental magma (e.g. Toplis & Carroll, 1995; Zhou *et al.*, 2005), timing of Fe–Ti oxide crystallization (e.g. Namur *et al.*, 2010) and oxygen fugacity (Toplis & Carroll, 1995). To provide some indications for mineral prospecting, a detailed study of the petrography and mineral compositions is needed to characterize the nature, liquid line of descent and oxygen fugacity of the Xiaohaizi wehrlite intrusion.

Here we present secondary ion mass spectrometry (SIMS) zircon U–Pb age data, *in situ* major and trace element compositions of cumulus clinopyroxenes, and Sr–Nd–Pb isotopic analyses of mineral separates and whole-rocks. The main objectives are (1) to characterize the nature of the parental magma and hence the mantle source of the Xiaohaizi wehrlite intrusion and to constrain its genetic relationship to the crosscutting dykes, and (2) to understand the role of the AFC process in the generation of LMI.

## GEOLOGICAL BACKGROUND

### Regional geology

The Tarim Craton in NW China is surrounded by the Tianshan orogenic belt to the north and NW, the Kunlun orogenic belt to the SW and the Altyn orogenic belt to the SE (Fig. 1a and b). The Tianshan orogenic belt is part of the Central Asian Orogenic Belt (CAOB), which is the largest Phanerozoic orogen in the world and has a complex evolutionary history represented by multi-stage subduction and juvenile crustal growth (Han *et al.*, 2011, and references therein). The basement of the Tarim Craton is composed mainly of (1) Archean tonalite–trondhjemitic–granodiorite (TTG) gneisses and amphibolites, (2) Palaeoproterozoic metamorphic mafic and felsic intrusions, schists and marbles, (3) Mesoproterozoic to early Neoproterozoic low-grade metamorphic rocks including metamorphosed carbonate and clastic rocks and granitoids, and (4) middle to late Neoproterozoic mafic dykes, bimodal volcanic rocks, granitoids and glacial deposits, which crop out along the margins of the craton (e.g. Kuluketage, Altyn and southwestern Tarim; BGMRXUAR, 1993; Hu *et al.*, 2000; Lu *et al.*, 2008). The basement is overlain by a thick sequence of Phanerozoic shallow marine and terrestrial sandstones, siltstones, shales, dark limestones, chert and volcanic rocks (BGMRXUAR, 1993; Cao *et al.*, 2011).

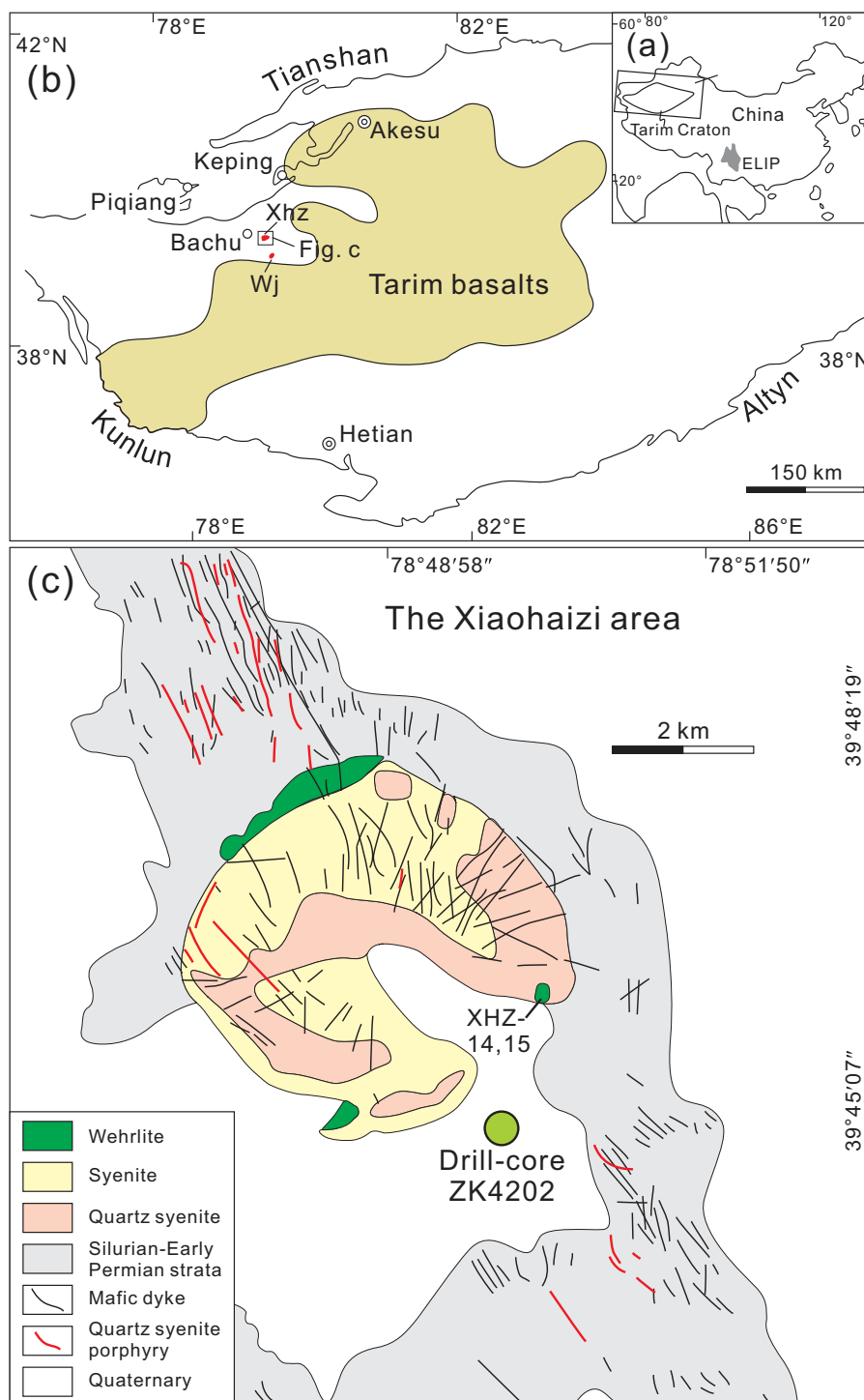


**Fig. 1.** (a) Locations of the Tarim Craton and Emeishan large igneous province (ELIP) and the study area (rectangle), modified after Zhou *et al.* (2009). (b) Simplified geological map of the Tarim Craton, showing the distribution of Permian Tarim basalts and ultramafic-felsic intrusive complexes around Bachu, modified after BGMRXUAR (1993) and Yang *et al.* (2007). Wj, Wajilitag mafic-ultramafic layered intrusion; Xhz, Xiaohaizi syenite complex. (c) Detailed geological map of the Xiaohaizi syenite, which is crosscut by numerous mafic and felsic dykes, modified after Yang *et al.* (2007) and Chen *et al.* (2010a). Also shown is the location of drill-core ZK4202 and wehlrite outcrops (XHZ-14 and XHZ-15).

Several episodes of igneous activity have been identified in the Tarim Craton, including those associated with the formation of the Neoproterozoic and Proterozoic basement, and early Permian flood basalts and ultramafic–mafic intrusions. Among these the early Permian magmatic event is the most extensive (Li *et al.*, 2008; Pirajno *et al.*, 2008; Zhang *et al.*, 2008a, 2010a, 2010b; Zhou *et al.*, 2009; Tian *et al.*, 2010; Yu *et al.*, 2011b). Geophysical surveys show that the Permian basalts may extend over an area of 250 000 km<sup>2</sup> in the interior of the craton (Yang *et al.*, 2007; Tian *et al.*, 2010). The early Permian basalts crop out mainly in the northwestern and southwestern parts of the craton, with significant exposures in the Keping area. Based on a compilation of published age data, the basaltic volcanism took place in the interval 292–286 Ma with a peak at 289 Ma (Wei *et al.*, 2014), and appears to originate from an SCLM source (Jiang *et al.*, 2004; Zhang *et al.*, 2010a; Wei *et al.*, 2014). Apart from the voluminous flood basalts a variety of small-volume, scattered mafic–ultramafic intrusions, syenites, mafic dykes and quartz syenite porphyries also crop out. They were formed mainly during the interval 278–284 Ma (Yang *et al.*, 1996, 2006, 2007; Zhang *et al.*, 2008a, 2010a; Li *et al.*, 2011b; Zhang & Zou, 2013b) with a peak age at ~279 Ma, and are interpreted to be derived from a connecting mantle source (Zhou *et al.*, 2009; Zhang *et al.*, 2010a; Zhang & Zou, 2013a; Wei *et al.*, 2014). A model involving mantle plume–lithosphere interaction has been proposed to account for the generation of the Tarim LIP (Wei *et al.*, 2014; Xu *et al.*, 2014). The basalts were formed by partial melting of the SCLM in response to the impact of a mantle plume at the base of thickened continental lithosphere beneath Tarim, whereas the dykes and intrusions were generated by decompression melting of the mantle plume as a result of its lateral deflection towards the margins of the Tarim Craton where the lithosphere is relatively thin (Wei *et al.*, 2014; Xu *et al.*, 2014).

### The Xiaohaizi cumulate wehrlite, syenite and dykes

The early Permian Xiaohaizi syenite complex is circular in shape and crops out about 28 km SE of Bachu city in the northwestern part of the Tarim Craton (Fig. 1b). It is composed predominantly of syenite and quartz syenite (Wei & Xu, 2011) and subordinate cumulate wehrlite (Fig. 1c). The wehrlites have previously been termed olivine gabbro (Wei & Xu, 2011, 2013) or olivine clinopyroxenite (Chen *et al.*, 2010a). In the field, the contact between the wehrlite and syenite is sharp (Fig. 2a). Within the eastern part of the syenite intrusion (Fig. 1c) irregular xenoliths of wehrlite occur adjacent to the contact (Fig. 2a), indicating that the wehrlites were intruded by the syenite. The wehrlites and syenites have a surface exposure of ~18 km<sup>2</sup>, and intrude Silurian–early Permian strata (BGMRXUAR, 1993). Previous investigations show that the Xiaohaizi

syenite was emplaced at 277–282 Ma (Yang *et al.*, 1996, 2006; Li *et al.*, 2007; Zhang *et al.*, 2009; Wei & Xu, 2011). The strata in this area include Silurian sandstone, siltstone and silty mudstone, Devonian conglomerate, sandstone and siltstone, Carboniferous sandstone, siltstone, gypsolith and limestone, and lower Permian limestone, silty mudstone and shale (Zhang, 2003). Numerous mafic dykes and quartz syenite porphyries crosscut the sedimentary rocks with nearly vertical dips and variable strikes and also intrude the Xiaohaizi syenite, although some of the dykes intermingle with the syenite (Zhang *et al.*, 2008b). These dykes have been dated at 278–284 Ma (Yu, 2009; Li *et al.*, 2011b), indistinguishable from the ages of the syenite intrusion.

A strong negative aeromagnetic anomaly in the Xiaohaizi area indicates the presence of a concealed mafic intrusion. This is supported by industrial drilling that revealed a large volume of mafic igneous rocks at depth. One drill-core (ZK4202) recovered about 750 m of cumulate wehrlite crosscut by numerous mafic dykes with sharp contacts (Fig. 2b). However, the bottom of the igneous sequence was not reached and the exact thickness of the cumulate wehrlites remains unknown.

The relative ages of the intrusive rocks can be obtained from crosscutting relationships. The oldest are the cumulate wehrlites, which are intruded by the Xiaohaizi syenite. Alkali basalt to trachyandesite dykes intrude the Silurian–early Permian strata, the Xiaohaizi wehrlites and the syenites. The youngest intrusions are the quartz syenite porphyries, which crosscut both the Xiaohaizi syenite and the mafic dykes (Chen *et al.*, 2010a).

## SAMPLE SELECTION AND ANALYTICAL METHODS

### Sample selection

Two coarse-grained mafic wehrlite samples from the top (4202-a) and bottom (4202-b) of the drill-core (ZK4202) were selected for zircon SIMS U–Pb dating. Twenty-two cumulate wehrlites and four fine-grained crosscutting dykes from the drill-core were selected for major and trace element analysis. All four dykes and 18 wehrlite samples were selected for Sr–Nd isotope analysis. Whole-rock Sr–Nd isotope analyses were carried out on seven wehrlites; clinopyroxene–plagioclase separates from three of these wehrlites were also analyzed. For the rest of the samples, only mineral separates were analyzed. Clinopyroxene and plagioclase mineral separates were handpicked under a binocular microscope to minimize the effect of alteration. Pb isotopes were also analyzed for plagioclase separates. Two wehrlites collected from the outcrop display relatively strong alteration and thus were analyzed only for trace elements.



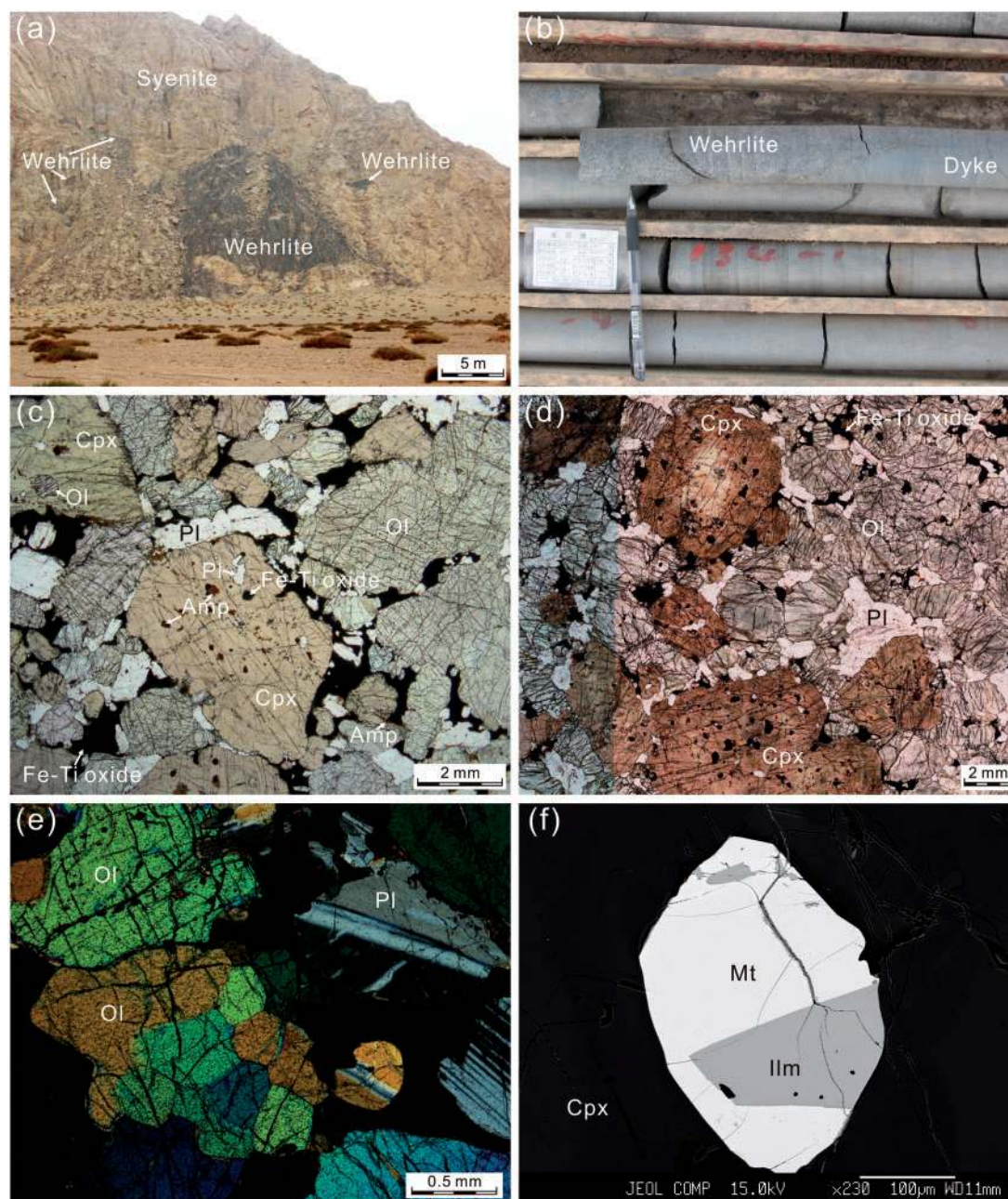


**Fig. 2.** (a) Field relationship between the Xiaohaizi wehlrite and the syenite intrusion. Wehlrite xenoliths occur within the syenite adjacent to the contact. (b) Crosscutting relationship between wehlrite and a dyke in the drill-core. (c–e) Photomicrographs showing mineral textures in the Xiaohaizi cumulate wehrlites. (c) Large cumulus clinopyroxene and olivine with small interstitial plagioclase and Fe–Ti oxides. Large, euhedral clinopyroxenes include small grains of plagioclase, Fe–Ti oxides and brown amphibole. A few Fe–Ti oxide grains are rimmed by brown amphibole or biotite (sample 4202-18; plane-polarized light). (d) Zonal structure of a large clinopyroxene grain (sample 4202-63; plane-polarized light). (e) Aggregates of small olivine grains with 120° triple junctions (sample 4202-41; cross-polarized light). (f) BSE image of coexisting magnetite and ilmenite included in clinopyroxene. Ol, olivine; Cpx, clinopyroxene; Pl, plagioclase; Mt, magnetite; Ilm, ilmenite.

### Analytical methods

Zircons extracted from rock samples for U–Pb isotope analysis were processed by conventional heavy liquid and magnetic separation techniques. Zircon grains, together with zircon standard 91500, were set in epoxy mounts,

which were then polished to expose the interior of the grains. They were then imaged by cathodoluminescence (CL) using a LEO 1450 VP (LEO Company, Germany) scanning electron microscope connected to a Mini CL system (Gatan Company, UK) at the Institute of Geology

and Geophysics, Chinese Academy of Sciences in Beijing (IGG-CAS), to characterize their internal structures and choose potential target sites for U–Pb dating. The imaging conditions were 15 kV and 1.1 nA, with a working distance of 26 mm.

Measurements of U, Th and Pb isotopes were conducted by SIMS using a Cameca IMS-1280 ion microprobe at IGG-CAS. Analytical procedures are the same as those described by Li *et al.* (2009). The  $\text{O}_2^-$  primary ion beam was accelerated at 13 kV, with an intensity of  $\sim 8$  nA. The ellipsoidal spot is about  $20\text{ }\mu\text{m} \times 30\text{ }\mu\text{m}$  in size. U, Th and Pb were analyzed at a mass resolution ( $M/\Delta M$ ) of  $\sim 5400$ . Pb ion yields were increased by a factor of  $\sim 2$  by flooding the sample surface with oxygen. Any effects from surface contamination were minimized by pre-rastering an  $\sim 20\text{ }\mu\text{m}$  surface area for 180 s prior to analysis. Each measurement consists of seven cycles, and the total analytical time is  $\sim 12$  min. U/Pb ratios were calibrated against measured ratios in zircon standard 91500 with an age of  $\sim 1065$  Ma and assuming a  $^{206}\text{Pb}/^{238}\text{U}$  ratio of 0.17917 (Wiedenbeck *et al.*, 1995). Standard analyses were carried out after every three unknown analyses. Calculated Th/U ratios in all unknown samples were obtained by comparison with measured Th/U ratios ( $\text{Th}/\text{U} = 0.362$ ) and  $^{206}\text{Pb}/^{238}\text{U}$  in zircon standard 91500 assuming closed-system behavior. A long-term uncertainty of 1.5% (1 RSD—Relative Standard Deviation) for  $^{206}\text{Pb}/^{238}\text{U}$  measurements of the standard zircons was propagated to the unknowns (Li *et al.*, 2010), despite the fact that the measured  $^{206}\text{Pb}/^{238}\text{U}$  error in a specific session was generally around 1% (1 RSD) or less. Measured compositions were corrected for common Pb using  $^{204}\text{Pb}$  correction. Corrections are sufficiently small to be insensitive to the choice of common Pb composition, and an average of present-day crustal composition (Stacey & Kramers, 1975) was used for the common Pb assuming that the common Pb is largely surface contamination introduced during sample preparation. Uncertainties on single analyses in the data tables are reported at the  $1\sigma$  level; mean ages for pooled U/Pb (and Pb/Pb) analyses are quoted at the 95% confidence interval. ISOPLOT (version 3) was used for plots and age calculations (Ludwig, 2003).

The fine-grained crosscutting dykes, clinopyroxene and plagioclase separates from the wehrlites were cleaned twice with 2% HCl, followed by twice with MiliQ water, and then powdered by hand in an agate mortar under a fume hood at the University of Queensland (UQ), Australia.

Major element analyses of minerals were obtained by electron microprobe analysis (EMPA) using a JEOL JXA-8100 Superprobe at the Guangzhou Institute of Geochemistry, Chinese Academy of Sciences (GIG-CAS). The accelerating voltage was set at 15 kV with a beam

current of 20 nA and a beam diameter of 1–2  $\mu\text{m}$ . The peak centering and counting duration was 20 s. The data reduction was carried out using ZAF correction procedures.

Whole-rock major element oxides were determined by standard X-ray fluorescence (XRF) techniques. Samples were prepared as glass discs using a Rigaku desktop fusion machine. Analyses were performed on a Rigaku ZSX100e instrument at GIG-CAS following the procedure described by Goto & Tatsumi (1996). Analytical uncertainties are mostly between 1 and 5%. Trace elements were determined at GIG-CAS by inductively coupled plasma mass spectrometry (ICP-MS) using a PE Elan 6000 system, following the procedures described by Liu *et al.* (1996), and at the University of Queensland (UQ) using a Thermo X-Series II ICP-MS system following the detailed procedures described by Wei *et al.* (2014), respectively. Precision and accuracy of trace element analyses are commonly within 5%. Standard rock measurements at UQ, together with reference values, are listed in Supplementary Data 1 (supplementary data are available for downloading at <http://www.petrology.oxfordjournals.org>).

Sr, Nd and Pb chemical separation was performed following a modified procedure described by Pin & Zalduegui (1997), Deniel & Pin (2001) and Míková & Denková (2007). Strontium was loaded on Ta filaments with  $\text{TaF}_5$  and measured fully automatically by thermal ionization mass spectrometry (TIMS) on a VG Sector 54 system at UQ in a three-sequence dynamic mode using  $^{86}\text{Sr}/^{88}\text{Sr} = 0.1194$  for exponential mass fractionation corrections. The NBS-987 standard was used as a monitor of the detector efficiency drift of the instrument. This was repeatedly measured during the analysis of the samples ( $n = 45$ ) and yielded an average of  $0.710222 \pm 20$  ( $2\sigma$ ). The deviation of this mean value from the laboratory's previously obtained long-term average of  $0.710249 \pm 28$  ( $2\sigma$ ) was used to correct all samples. Nd isotopes were analyzed fully automatically by multi-collector inductively coupled plasma mass spectrometry (MC-ICP-MS) using a Nu Plasma system at UQ, using a three-sequence dynamic procedure. Instrument bias and mass fractionation were corrected for by normalizing the raw ratios to  $^{146}\text{Nd}/^{144}\text{Nd} = 0.7219$ . Eleven measurements of the JNdi-1 standard yielded an average of  $^{143}\text{Nd}/^{144}\text{Nd} = 0.512113 \pm 9$  ( $2\sigma$ ,  $n = 11$ ), which is consistent with the reported value of  $0.512115 \pm 7$  (Tanaka *et al.*, 2000). Seventeen analyses of an in-house laboratory standard Ames Nd Metal yielded an average of  $^{143}\text{Nd}/^{144}\text{Nd} = 0.511966 \pm 16$  ( $2\sigma$ ). This value was used as a calibration reference to monitor instrument drift, which is usually less than 15 ppm. Lead separated from column chemistry was doped with 4 ppb thallium with a  $^{205}\text{Tl}/^{203}\text{Tl}$  ratio of 0.23875 was used for mass fractionation correction. Pb isotopes were analyzed fully automatically by MC-ICP-MS using the Nu Plasma system at UQ. Repeated analyses of NBS 981 yielded average ratios



of  $^{208}\text{Pb}/^{204}\text{Pb} = 36.705 \pm 14$ ,  $^{207}\text{Pb}/^{204}\text{Pb} = 15.494 \pm 4$  and  $^{206}\text{Pb}/^{204}\text{Pb} = 16.936 \pm 5$  ( $n = 38$ ,  $2\sigma$ ). Lead isotope data are reported relative to NBS 981 values of  $^{208}\text{Pb}/^{204}\text{Pb} = 36.718$ ,  $^{207}\text{Pb}/^{204}\text{Pb} = 15.494$  and  $^{206}\text{Pb}/^{204}\text{Pb} = 16.941$  (Collerson *et al.*, 2002).

*In situ* trace element analyses of clinopyroxenes from the Xiaohaizi wehrlites were made by laser ablation (LA)-ICP-MS using an Agilent 7500a ICP-MS system coupled with a Resolution M50-HR 193 nm ArF-excimer laser sampler, following the analytical procedure described by Tu *et al.* (2011). The laser operated at a repetition rate of 10 Hz, and the spot diameter was 53  $\mu\text{m}$ . Ablation signal and integration intervals were selected by careful inspection of the time-resolved analysis to ensure that no inclusions were present in the analyzed volume. Calibration was carried out externally using NIST SRM 612 and KL 2 with  $^{44}\text{Ca}$  as an internal standard. Repeated analyses of NIST 612 and KL 2 indicate that precision and accuracy are both better than 4% for most elements. For Cpx, the relative standard deviations (RSD) of most elements are better than 5%.

## PETROGRAPHY OF THE STUDIED SAMPLES

The cumulate wehrlites are massive, coarse-grained rocks without prominent layering; from the bottom to the top of the core, the amount of mafic minerals is relatively uniform. Clinopyroxene commonly appears as very large grains ( $>5\text{ mm}$ ) and a single thin section may contain only several clinopyroxene grains (Supplementary Fig. 1). It is, therefore, very difficult to obtain modal proportions by point counting. Normative compositions are therefore calculated from bulk-rock compositions and constituent mineral compositions using a least-squares regression method. The mineral mode determined this way is slightly different from that obtained by point counting (Supplementary Dataset 2). Olivine ( $\sim 22\text{--}55\%$ ) and clinopyroxene ( $\sim 28\text{--}42\%$ ) are the most abundant cumulus phases, whereas plagioclase ( $\sim 5\text{--}8\text{--}25\%$ ) and Fe–Ti oxides ( $\sim 6\text{--}19\%$ ) are subordinate, occurring interstitially between clinopyroxene and olivine (Fig. 2c and d).

Olivine occurs as large (up to 5 mm), slightly prismatic subhedral grains or aggregates of smaller grains ( $<0.2\text{ mm}$ ). The olivine aggregates commonly display triple junctions with  $\sim 120^\circ$  interfacial angles (Fig. 2e), a texture considered to indicate subsolidus recrystallization (e.g. Duchesne & Charlier, 2005). Clinopyroxene is commonly pinkish in color and occurs as very large (up to 15 mm) euhedral to anhedral grains, often containing abundant Fe–Ti oxides, plagioclase and rarely olivine inclusions (Fig. 2c). Some clinopyroxene grains display prominent normal zoning from core to rim (Fig. 2d). Other clinopyroxene grains exhibit patchy replacement by

brown amphibole or biotite. Plagioclase has a grain size ranging from 0.1 to 2 mm, forming subequant to strongly tabular subhedral to euhedral grains (Fig. 2c and d); no zoning in plagioclase was observed. In all samples plagioclase inclusions are found within clinopyroxenes, indicating that the two minerals crystallized simultaneously. These plagioclase inclusions are smaller than the unenclosed plagioclase crystals (Fig. 2c and d). Fe–Ti oxide minerals are anhedral magnetite and minor ilmenite. They occur either as small ( $<3\text{ mm}$ ) interstitial patches between the silicate minerals or as tiny inclusions ( $<400\text{ }\mu\text{m}$ ) in the silicate minerals (Fig. 2c and d). A few Fe–Ti oxide grains are rimmed by brown amphibole (Fig. 2c).

Wehrlites from the surface outcrop show identical textures to the drill-core wehrlites but are strongly altered with clinopyroxene and plagioclase transformed to chlorite and sericite (Supplementary Fig. 2a).

The dykes are fine-grained with a small proportion of plagioclase phenocrysts ( $<1\%$ ) (Supplementary Fig. 2b). The groundmass contains plagioclase ( $\sim 60\%$ ), clinopyroxene ( $\sim 30\%$ ), Fe–Ti oxides ( $\sim 10\%$ ) and minor biotite.

## RESULTS

### Zircon U–Pb dating

Cumulate wehrlite samples 4202-a and 4202-b from the top and bottom of the drill-core ZK4202, respectively, were selected for zircon U–Pb dating. Most zircons are 100–250  $\mu\text{m}$  in length, with aspect ratios between 1:1 and 2:1, euhedral to subhedral and transparent with no evident inclusions. CL images of zircons show strong oscillatory zoning with prominent sector zoning (Fig. 3a and b), indicating a magmatic origin.

Zircons from sample 4202-a have low Th and U contents (39–250 ppm and 44–165 ppm, respectively) with relatively high Th/U ratios of 0.62–1.61 (Table 1). Common Pb is generally low; values for  $f_{206}$  (the proportion of common  $^{206}\text{Pb}$  in total measured  $^{206}\text{Pb}$ ) is lower than 0.4%. All 16 analyses are concordant in  $^{206}\text{Pb}/^{238}\text{U}$  and  $^{207}\text{Pb}/^{235}\text{Pb}$  within analytical error (Fig. 3c), yielding a concordia age of  $278.9 \pm 2.1\text{ Ma}$  ( $2\sigma$ , MSWD of concordance = 0.20, 95% confidence level, probability of confidence = 0.65).

Zircons from sample 4202-b have low Th and U contents (26–133 ppm and 29–108 ppm, respectively) with high Th/U ratios of 0.62–1.23 and low common Pb ( $f_{206} < 0.6\%$ , Table 1). Sixteen analyses have very similar apparent  $^{207}\text{Pb}/^{235}\text{U}$  and  $^{206}\text{Pb}/^{238}\text{U}$  ages, and define a concordant age of  $278.4 \pm 2.1\text{ Ma}$  ( $2\sigma$ , MSWD of concordance = 0.008, 95% confidence level, probability of confidence = 0.93; Fig. 3d).

Both samples from the top and bottom of the drill-core ZK4202 yield consistent SIMS zircon U–Pb ages of  $\sim 279\text{ Ma}$ . However, the zircons clearly did not form at the same time as the mafic minerals because zircon does

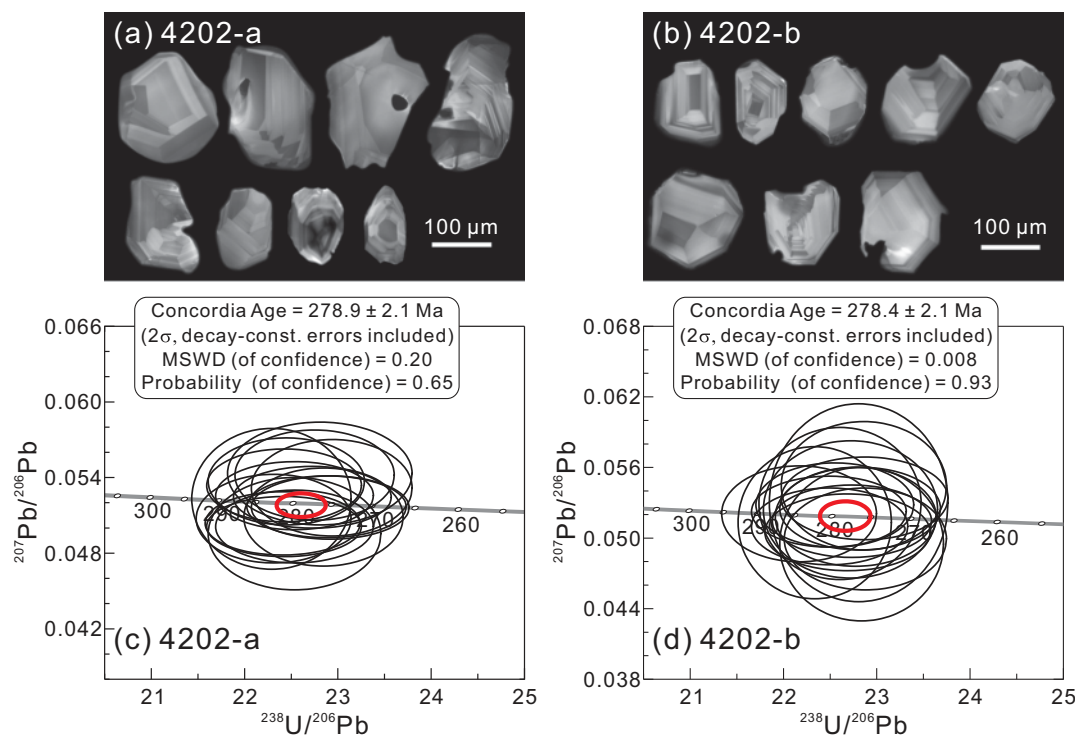


**Fig. 3.** Cathodoluminescence (CL) images (a, b) for typical zircons and Tera–Wasserburg plots (c, d) for SIMS zircon U–Pb chronology of the Xiaohaizi cumulate wehrlites (4202-a and 4202-b from the top and bottom of drill-core ZK4202, respectively).

not crystallize from mafic–ultramafic melts, but only from more evolved magmas. The zircons could have formed from the remaining magma after segregation of the mafic minerals or from another batch of more evolved magma of the same magmatic phase. In this case, the zircon age gives only a minimum age for the Xiaohaizi wehrlites. Nevertheless, the time lag between the mafic cumulate formation and the crystallization of the zircons may be small, probably within the uncertainty of the ages.

## Mineral chemistry

### Major elements

Major element compositions for olivine (171 analyses on 159 grains), clinopyroxene (428 analyses on 266 grains), plagioclase (278 analyses on 278 grains), magnetite (251 analyses on 251 grains) and ilmenite (63 analyses on 63 grains) in the cumulate wehrlites are presented in Supplementary Datasets 3–6.

Olivine has a relatively uniform composition in each sample. The olivine Fo [ $100 \times \text{atomic Mg}^{2+}/(\text{Mg}^{2+} + \text{Fe}^{2+})$ ] content in the wehrlites varies from 69 to 75 (Supplementary Dataset 3). No significant zoning (i.e.  $>2$  in Fo content) is observed in single olivine crystals; NiO abundances range from 0.03 to 0.24 wt %. Olivines in the wehrlite from the surface outcrop samples

display identical compositions to those of the drill-core samples.

Clinopyroxenes in the wehrlites are diopside in composition (Fig. 4a) with Mg# [ $100 \times \text{atomic Mg}^{2+}/(\text{Mg}^{2+} + \text{Fe}^{2+})$ ] ranging from 75 to 84 (Supplementary Dataset 4). Clinopyroxene compositions fall within the field for alkaline basalts (Fig. 4b). Variation of Mg# within a single grain of clinopyroxene is generally small ( $<1.5$ ) for grains less than 5 mm, but for three relatively larger grains ( $>5$  mm) (see Supplementary Fig. 3 for details) the variation can be up to seven. The spread of  $\text{Al}_2\text{O}_3$  and  $\text{TiO}_2$  contents within all clinopyroxene grains is wide (2.01–5.47 wt % and 0.69–2.20 wt %, respectively) and is negatively correlated with Mg# (for  $\text{Mg}\# > 78$ ) (Fig. 5a and b). A weak negative trend can also be seen on an Mg# vs Na variation plot at  $\text{Mg}\# > 78$  (not shown).  $\text{Cr}_2\text{O}_3$  contents are up to 1.05 wt %. In contrast, CaO contents are relatively constant. No apparent correlation exists between CaO,  $\text{Cr}_2\text{O}_3$  and Mg# (Fig. 5c and d).

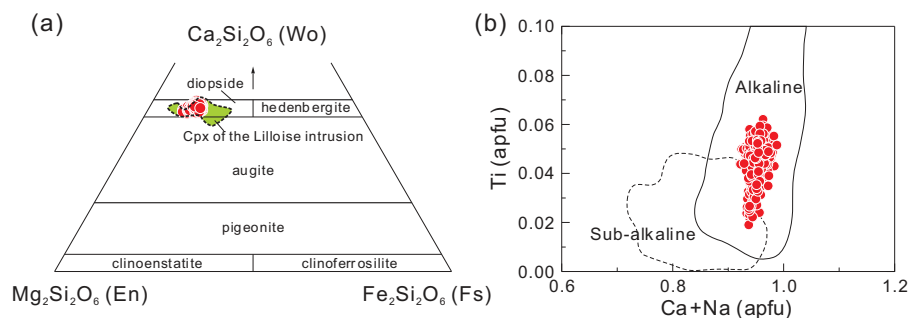
Plagioclase in the wehrlites shows wide compositional variations with An content [ $= 100\text{Ca}/(\text{K} + \text{Na} + \text{Ca})$ ] ranging from 53 to 86 (Supplementary Dataset 5). Some intercumulus grains display normal zoning. Plagioclase inclusions in clinopyroxene display similar variations (55–83) in An content to the interstitial plagioclase (53–86). Plagioclase inclusions typically occur within



Table 1: SIMS zircon U–Pb data for the Xiaohaizi cumulate wehrlites

Spot	U	Th	Th/U	<sup>206</sup> Pb/ <sup>204</sup> Pb	f <sub>206</sub>	Ratio	Age (Ma)				Correlation coefficient							
							<sup>207</sup> Pb/ <sup>206</sup> Pb	±1σ (%)	<sup>206</sup> Pb/ <sup>238</sup> U	±1σ (%)	<sup>207</sup> Pb/ <sup>235</sup> U	±1σ	<sup>206</sup> Pb/ <sup>238</sup> U	±1σ				
4202-a																		
1	83	88	1.06	9321	0.20	0.0531	2.93	0.3191	3.30	0.0436	1.53	332.6	65.0	281.2	8.1	275.1	4.1	0.46
2	44	41	0.93	n.a.	0.00	0.0522	4.38	0.3228	4.65	0.0448	1.56	294.5	97.0	284.1	11.6	282.8	4.3	0.34
3	155	250	1.61	14823	0.13	0.0524	1.95	0.3177	2.47	0.0440	1.51	301.5	43.9	280.1	6.1	277.6	4.1	0.61
4	128	111	0.87	n.a.	0.00	0.0500	1.93	0.3075	2.45	0.0446	1.52	195.9	44.2	272.2	5.9	281.2	4.2	0.62
5	73	61	0.83	n.a.	0.00	0.0542	2.70	0.3281	3.10	0.0439	1.53	377.5	59.5	288.1	7.8	277.2	4.2	0.49
6	57	80	1.40	6972	0.27	0.0495	3.70	0.3027	4.06	0.0444	1.68	171.1	84.1	268.5	9.6	279.8	4.6	0.41
7	157	203	1.30	19191	0.10	0.0503	2.03	0.3094	2.53	0.0446	1.51	208.5	46.5	273.7	6.1	281.4	4.2	0.60
8	48	39	0.82	7999	0.23	0.0543	3.09	0.3281	3.56	0.0438	1.78	382.7	68.0	288.1	9.0	276.6	4.8	0.50
9	94	100	1.06	25637	0.07	0.0533	2.22	0.3278	2.69	0.0446	1.52	342.7	49.6	287.9	6.8	281.2	4.2	0.56
10	165	163	0.99	12909	0.14	0.0515	2.01	0.3100	2.52	0.0436	1.51	265.3	45.6	274.1	6.1	275.2	4.1	0.60
11	136	201	1.47	5731	0.33	0.0507	2.84	0.3131	3.22	0.0448	1.52	225.6	64.4	276.6	7.8	282.7	4.2	0.47
12	73	104	1.42	8826	0.21	0.0508	3.13	0.3067	3.48	0.0438	1.53	233.3	70.6	271.6	8.3	276.1	4.1	0.44
13	116	97	0.84	9373	0.20	0.0501	2.37	0.3062	2.82	0.0444	1.54	197.5	54.1	271.2	6.7	279.9	4.2	0.54
14	152	225	1.48	18648	0.10	0.0517	1.95	0.3113	2.47	0.0437	1.52	270.7	44.1	275.2	6.0	275.7	4.1	0.61
15	65	72	1.11	11137	0.17	0.0536	2.65	0.3290	3.06	0.0445	1.54	353.3	58.7	288.8	7.7	280.9	4.2	0.50
16	107	67	0.62	29279	0.06	0.0525	2.09	0.3211	2.59	0.0444	1.52	307.2	47.0	282.8	6.4	279.8	4.2	0.59
4202-b																		
1	36	28	0.78	4366	0.43	0.0529	5.02	0.3222	5.26	0.0442	1.57	322.8	110.1	283.6	13.1	278.9	4.3	0.30
2	108	133	1.23	7326	0.26	0.0504	2.65	0.3064	3.10	0.0441	1.60	215.0	60.4	271.4	7.4	278.0	4.3	0.52
3	82	98	1.20	22113	0.08	0.0514	2.42	0.3114	2.86	0.0440	1.53	257.4	54.7	275.3	6.9	277.4	4.2	0.53
4	83	99	1.19	13933	0.13	0.0521	2.38	0.3196	2.82	0.0445	1.51	292.0	53.6	281.6	7.0	280.4	4.1	0.53
5	47	54	1.16	3182	0.59	0.0512	5.14	0.3161	5.36	0.0448	1.51	250.6	114.2	278.9	13.2	282.3	4.2	0.28
6	50	59	1.18	13635	0.14	0.0524	4.56	0.3182	4.86	0.0440	1.68	303.9	100.8	280.5	12.0	277.7	4.6	0.35
7	68	42	0.62	n.a.	0.00	0.0509	2.66	0.3120	3.07	0.0444	1.53	237.5	60.1	275.8	7.4	280.3	4.2	0.50
8	74	48	0.64	6060	0.31	0.0520	3.19	0.3232	3.54	0.0451	1.53	284.1	71.4	284.3	8.8	284.4	4.2	0.43
9	49	60	1.21	8361	0.22	0.0529	6.51	0.3198	6.74	0.0438	1.72	324.3	141.5	281.7	16.7	276.6	4.7	0.26
10	44	31	0.70	n.a.	0.00	0.0517	3.35	0.3133	3.70	0.0439	1.55	274.1	75.0	276.7	9.0	277.0	4.2	0.42
11	42	38	0.91	3145	0.59	0.0494	5.38	0.2984	5.60	0.0438	1.56	168.2	121.1	265.1	13.2	276.2	4.2	0.28
12	29	26	0.90	7304	0.26	0.0544	4.11	0.3277	4.40	0.0437	1.58	386.1	89.7	287.8	11.1	275.8	4.3	0.36
13	65	51	0.78	10444	0.18	0.0524	2.76	0.3168	3.16	0.0438	1.54	304.1	61.6	279.4	7.7	276.5	4.2	0.49
14	72	71	1.00	11378	0.16	0.0527	2.77	0.3222	3.17	0.0443	1.53	316.0	61.9	283.6	7.9	279.7	4.2	0.48
15	57	35	0.62	14344	0.13	0.0499	3.54	0.3006	3.86	0.0437	1.55	189.6	80.3	266.9	9.1	275.8	4.2	0.40
16	87	60	0.69	n.a.	0.00	0.0533	2.72	0.3213	3.16	0.0437	1.60	341.6	60.5	282.9	7.8	275.8	4.3	0.51

 $f_{206}$  is the percentage of common  $^{206}\text{Pb}$  in total  $^{206}\text{Pb}$ . n.a., not analyzed.



**Fig. 4.** Clinopyroxene compositions in the Xiaohaizi cumulate wehrlites. (a) Pyroxene quadrilateral (Morimoto *et al.*, 1988) showing that most clinopyroxene analyses fall in the diopside field. Clinopyroxene compositions in the Xiaohaizi wehrlites are similar to those of the Lilloise intrusion, East Greenland (Chambers & Brown, 1995). (b) Variation between Ti and Ca + Na cations (a.p.f.u.; atoms per formula unit) showing that most clinopyroxenes are similar to those in alkali basalts (Leterrier *et al.*, 1982). Cpx, clinopyroxene.

clinopyroxenes with  $Mg\# < 79$ . No correlation exists between the  $Mg\#$  of clinopyroxene and the An content of plagioclase regardless of whether the grains are interstitial or inclusions (Fig. 5e and f).

Magnetite ranges from near end-member  $Fe_3O_4$  to titanomagnetite containing up to 16.3 wt %  $TiO_2$  (Supplementary Dataset 6).  $Al_2O_3$  ranges from 0.54 to 10.5 wt % and  $MgO$  from 0.19 to 4.44 wt %; the upper ends of these ranges are typical of magnetites from alkali basalts (Frost & Lindsley, 1991).  $Cr_2O_3$  contents of magnetite inclusions hosted in olivine, clinopyroxene and plagioclase show a wider range (0.51–11.9 wt %) than in the interstitial magnetite (0.46–3.69 wt %).

Ilmenite ranges from end-member  $FeTiO_3$  to ferrian ilmenite containing 11.9 wt %  $Fe_2O_3$  (Supplementary Dataset 6).  $MgO$  contents range from 1.37 to 8.53 wt % and  $MnO$  from 0.39 to 1.04 wt %.  $Cr_2O_3$  is very low, up to 0.18 wt %.

The stratigraphic variations in olivine and magnetite composition in the drill-core are illustrated in Fig. 6b and c.  $NiO$  contents in olivine and  $Cr_2O_3$  contents in magnetite decrease systematically from the base upwards.

**Trace elements.** Trace element data obtained by LA-ICP-MS for clinopyroxenes of the cumulate wehrlites are given in Supplementary Dataset 4. Clinopyroxenes display convex chondrite-normalized rare earth element (REE) patterns with negligible Eu anomalies (0.9–1.1, Fig. 7a, Supplementary Dataset 4). In primitive mantle-normalized trace element patterns (Fig. 7b), Nb, Sr, Zr and Hf are depleted relative to neighboring REE. Th is highly variable; in some clinopyroxenes, Th is enriched over Nb, whereas in the others Th is depleted. This could be ascribed to poor analytical precision for Th and Nb because the concentrations of these elements in some samples are close to the detection limit. There is a good agreement between trace element compositions obtained

by dissolution of mineral separates (Supplementary Dataset 7) and *in situ* analyses (Fig. 7).

The trace element compositions of the clinopyroxenes bear strong resemblance to those of the clinopyroxene phenocrysts in the Emeishan high-Ti basalts (Fig. 7; Kamenetsky *et al.*, 2012). We have calculated the trace element composition of the hypothetical liquids in equilibrium with the least evolved ( $Mg\# > 80$ ) clinopyroxenes, using partition coefficients between clinopyroxene and melt (*D*) taken from Hauri *et al.* (1994) and Norman *et al.* (2005), for clinopyroxenes with similar major element compositions to the clinopyroxenes from the wehrlites. The calculated melts are characterized by highly enriched light REE (LREE) patterns [ $(La/Yb)_N = 14$ –27;  $(Dy/Yb)_N = 1.6$ –2.9; Supplementary Dataset 8] and enrichment in incompatible trace elements, (e.g. Th, U and high field strength elements) similar to those of average ocean island basalt (OIB; Sun & McDonough, 1989) and Emeishan high-Ti basalts (Fig. 7; Kamenetsky *et al.*, 2012).

### Whole-rock chemistry

Major and trace element data for representative whole-rock samples are given in Table 2. All the samples analyzed for major and trace elements are relatively fresh and have loss on ignition (LOI) values lower than 2.0 wt % (except for sample 4202-16). The wehrlites have relatively low  $SiO_2$  (36.33–41.68 wt %) and  $Al_2O_3$  (3.61–9.98 wt %), high  $MgO$  (13.55–24.44 wt %) and  $Fe_2O_3T$  (19.42–25.34 wt %), with  $Mg\#$  varying between 55 and 69 (Table 2).  $Na_2O$  and  $K_2O$  range from 0.29 to 1.04 wt % and from 0.02 to 0.34 wt %, respectively; whereas  $CaO$  contents show a relatively narrow range between 8.04 and 12.49 wt %. The wehrlites have very low contents of  $P_2O_5$  (0.01–0.03 wt %), except for sample 4202-49 ( $P_2O_5 = 0.11$  wt %). In Harker variation diagrams (Fig. 8),  $TiO_2$ ,  $Al_2O_3$ ,  $Fe_2O_3T$  and  $CaO$  increase with decreasing  $MgO$ . Sample 4202-39 has the highest  $Al_2O_3$  (9.98 wt %) and  $CaO$  (12.49 wt %), in keeping with the high mode of

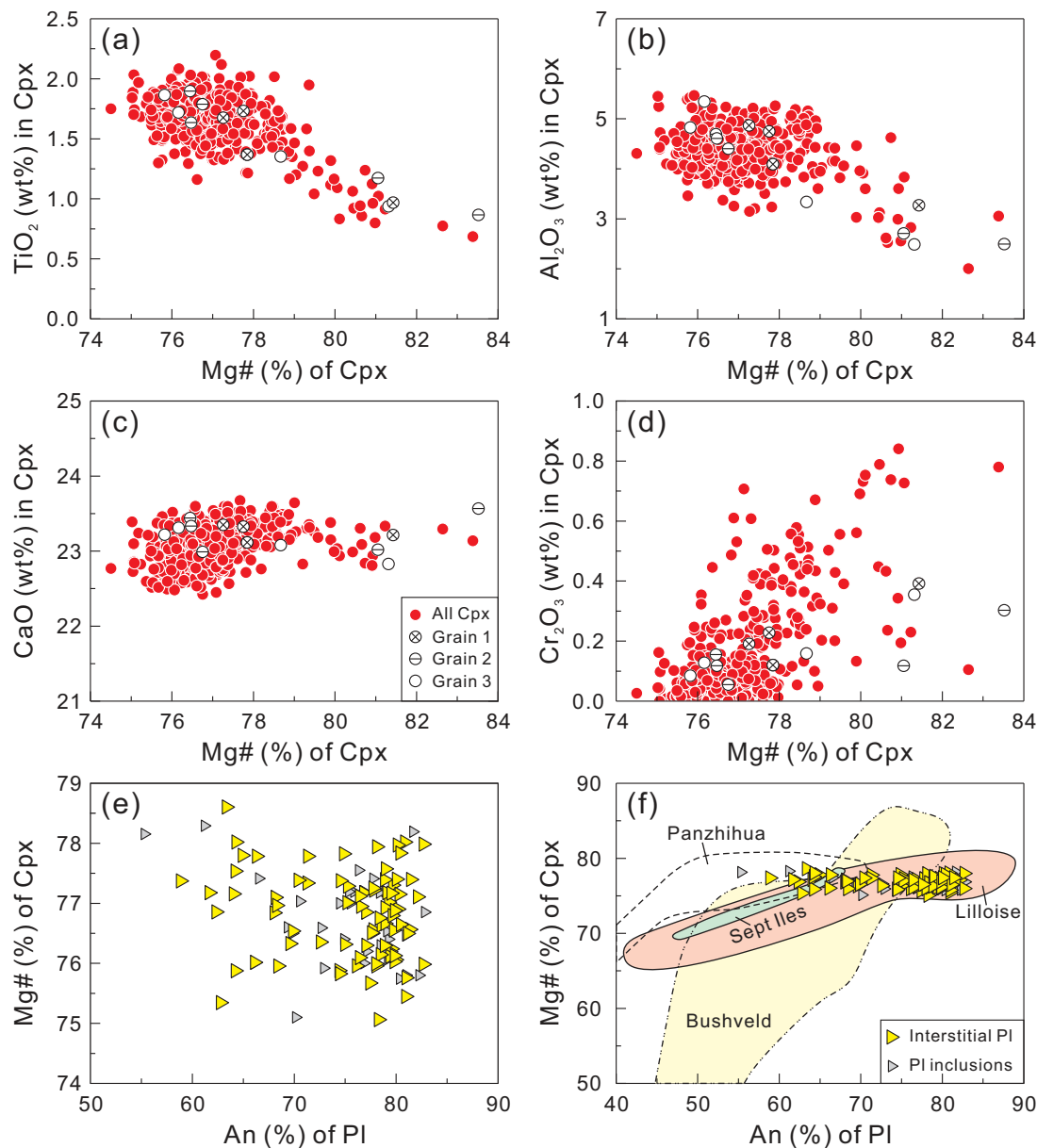


**Fig. 5.** Variation of TiO<sub>2</sub> (a), Al<sub>2</sub>O<sub>3</sub> (b), CaO (c) and Cr<sub>2</sub>O<sub>3</sub> (d) in clinopyroxene vs Mg# and Mg# of coexisting clinopyroxene (e, f) vs An content of plagioclase for the Xiaohaizi cumulate wehrlites. In (a)–(d) grain 1 from sample 4202-55, grain 2 from 4202-63 and grain 3 from 4202-64 (see Supplementary Data Fig. 3 for details) are distinguished from all the other analyses. In (f) fields of An–Mg# variation are shown for the Panzhihua intrusion (Pang *et al.*, 2009), Bushveld Complex (Ashwal *et al.*, 2005; Tegner *et al.*, 2006), Sept Iles intrusion (Namur *et al.*, 2011) and Lilloise intrusion (Chambers & Brown, 1995) for comparison. It should be noted that the Xiaohaizi wehrlites overlap with the middle olivine–pyroxene–plagioclase cumulate zone of the Lilloise intrusion. Cpx, clinopyroxene; Pl, plagioclase; An, anorthite content.

interstitial plagioclase in this sample (Supplementary Dataset 2).

The dykes crosscutting the wehrlites have low Mg# values of 35–39, with TiO<sub>2</sub> contents ranging from 1.68 to 2.94 wt % (Table 2). Compared with the wehrlites, they have higher SiO<sub>2</sub> (50.35–56.25 wt %) and Al<sub>2</sub>O<sub>3</sub> (14.02–16.41 wt %), but lower Fe<sub>2</sub>O<sub>3</sub>T (8.55–12.36 wt %). Na<sub>2</sub>O

and K<sub>2</sub>O vary from 3.51 to 4.68 wt % and from 1.60 to 2.89 wt %, respectively. On a volatile-free total alkalis–SiO<sub>2</sub> (TAS; Le Bas *et al.*, 1986) diagram (Fig. 9), the dykes show alkaline affinities. On plots of major element oxides against MgO (Fig. 8), TiO<sub>2</sub>, Fe<sub>2</sub>O<sub>3</sub>T and CaO decrease, whereas Al<sub>2</sub>O<sub>3</sub> increases with decreasing MgO. The dykes have very low concentrations of Ni (0.89–5.11 ppm)

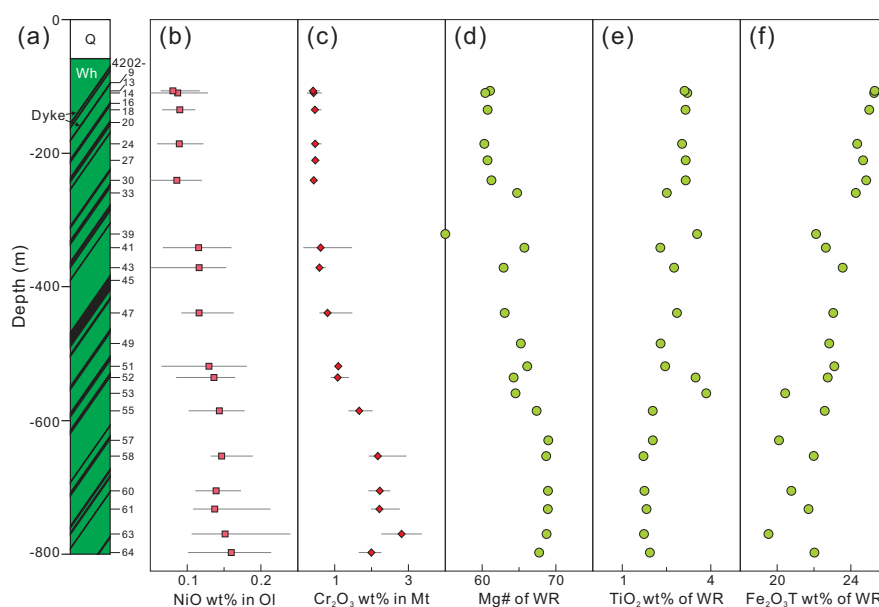


**Fig. 6.** (a) Schematic cross-section of the Xiaohaizi cumulate wehrlites from the drill-core (ZK4202) showing the total thickness investigated in this study, the distribution of dykes and the positions of analysed samples; (b–f) stratigraphic variations in mineral and whole-rock compositions within the Xiaohaizi wehrlites. (b) NiO content in olivine; (c)  $\text{Cr}_2\text{O}_3$  content in magnetite; (d) Mg# of whole-rocks; (e)  $\text{TiO}_2$  content of whole-rocks; (f)  $\text{Fe}_2\text{O}_3\text{T}$  content of whole-rocks. Data points for minerals represent average values. Ol, olivine; Mt, magnetite; WR, whole-rock; Q, Quaternary; Wh, wehlrite.

and Cr (0.06–3.81 ppm) (Table 2), suggesting that their parental magmas had experienced significant olivine and Fe–Ti oxide fractionation.

The chondrite-normalized REE patterns of the wehrlites are subparallel, characterized by a slight enrichment of the LREE over the heavy REE (HREE) [ $(\text{La}/\text{Yb})_{\text{N}} = 2.8\text{--}7.3$  with Yb enrichment ranging from 2.4 to 4.4 times chondrite; Fig. 10a]. The REE patterns of these samples display a weak–moderate positive Eu anomaly ( $\text{Eu}/\text{Eu}^* = 1.03\text{--}1.23$ ), which may reflect the role of plagioclase accumulation in their genesis. In primitive mantle-normalized trace element patterns (Fig. 10b), Ba, Ta, Sr and Ti typically display positive anomalies compared with the neighboring elements. The wehrlites are characterized by Th–U depletion and striking P depletion. The positive Sr and Ti anomalies may indicate plagioclase and Fe–Ti oxide accumulation. The wehrlites have low concentrations of incompatible elements (e.g.  $\text{P}_2\text{O}_5$ , REE, Zr) consistent with a cumulus origin. Sample 4202-49 displays the highest concentration of LREE. The presence of veins composed of fine-grained plagioclase, clinopyroxene and amphibole (Supplementary Fig. 2c) may contribute to this LREE enrichment. Wehrlites from the surface outcrops show similar REE and trace element patterns to sample 4202-49 (Fig. 10). Therefore, we consider that the wehrlites from the outcrop and the drill-cores belong to the same intrusion.

The dykes display strong enrichment in LREE relative to HREE (Fig. 10a) with  $(\text{La}/\text{Yb})_{\text{N}}$  up to 19.2 and weak Eu anomalies ( $\text{Eu}/\text{Eu}^* = 0.95\text{--}1.03$ ; Table 2). All samples

have similar trace element patterns, resembling OIB (Sun & McDonough, 1989; Fig. 10b) and the high-Ti basalts from the Emeishan LIP (Fig. 7, Kamenetsky *et al.*, 2012). All the samples except sample 4202-16 have Nb/U (36.5–46.8) and Ce/Pb (18.2–37.8) ratios similar to those of mantle-derived melts (Hofmann, 2003).

### Sr–Nd–Pb isotopic compositions

Sr–Nd isotope data (Table 3) were obtained for whole-rocks, clinopyroxene and plagioclase mineral separates from the wehrlites; Pb isotope data were obtained for the plagioclase separates (Table 4). The dykes are relatively fresh in thin section (Supplementary Fig. 2b) and have low LOI (Table 2), thus their Sr–Nd isotope compositions can be considered representative of the unaltered compositions. Only fresh and transparent parts of clinopyroxene and plagioclase grains were handpicked and analyzed, thus the effects of alteration are minimized. In addition, plagioclase usually has negligible Rb compared with Sr (Table 3) and thus the age-corrected initial Sr isotope composition is less sensitive to Rb mobility. Some wehlrite samples display local alteration of clinopyroxene, olivine and plagioclase (Supplementary Fig. 2d and e), thus Rb could be mobile during alteration and the age-corrected  $^{87}\text{Sr}/^{86}\text{Sr}$  of the whole-rocks could be slightly affected.

Initial isotopic compositions for the Xiaohaizi wehrlites and the crosscutting dykes were age corrected to 279 Ma (see Discussion section for justification for choice of ages). The wehrlites have uniform  $^{87}\text{Sr}/^{86}\text{Sr}_i$  (0.7042–0.7043) and slightly positive  $\epsilon_{\text{Nd}_i}$  values (0.8–1.1) (Table 3; Fig. 11a



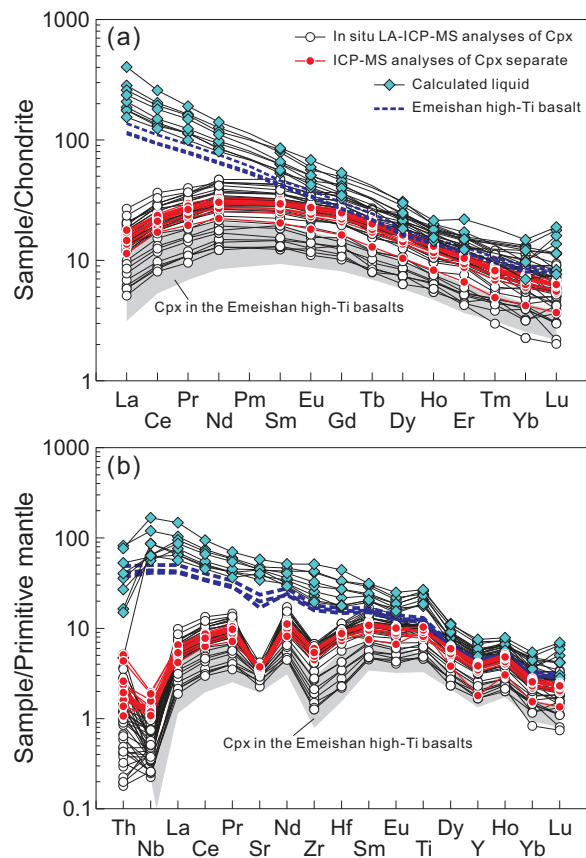


**Fig. 7.** Chondrite-normalized REE patterns (a) and primitive mantle-normalized multi-element patterns (b) for clinopyroxenes (*in situ* LA-ICP-MS analyses) and clinopyroxene separates (ICP-MS analyses on total dissolution of 50 mg material) of the Xiaohaizi cumulate wehrlites. Also shown for comparison is a field for clinopyroxenes from the Emeishan high-Ti basalts (Kamenetsky *et al.*, 2012). The compositions of the hypothetical liquids in equilibrium with less evolved ( $Mg\# > 80$ ) clinopyroxenes were calculated using partition coefficients from Hauri *et al.* (1994) and Norman *et al.* (2005). Chondrite and primitive mantle normalization values are from McDonough & Sun (1995).

and b). Clinopyroxene separates from the wehrlites display relatively lower  $^{87}Sr/^{86}Sr_i$  (0.7038–0.7041) and higher  $\epsilon Nd_i$  (1.0–1.9) values than those of the respective whole-rocks. Plagioclase separates have nearly constant  $^{87}Sr/^{86}Sr_i$  (0.7042–0.7043) and  $\epsilon Nd_i$  (0.4–1.0) values that are similar to those of the whole-rocks. The intermediate  $\epsilon Nd_i$  values of the whole-rocks could be accounted for by a mixture of clinopyroxene and plagioclase. The whole-rocks have comparable  $^{87}Sr/^{86}Sr_i$  to the plagioclase separates (Table 3, Fig. 11b) and deviate from the possible mixing trend between clinopyroxene and plagioclase. The shift of whole-rock  $^{87}Sr/^{86}Sr_i$  towards higher values can be ascribed to alteration. Plagioclase  $^{206}Pb/^{204}Pb_i$  ranges from 17.46 to 17.69,  $^{207}Pb/^{204}Pb_i$  from 15.47 to 15.50 and  $^{208}Pb/^{204}Pb_i$  from 37.81 to 37.95 (Table 4, Fig. 11c and d). The Pb isotope compositions of plagioclase are

systematically lower than those of the least contaminated dykes in the Xiaohaizi area, but similar to those of the Keping basalts (Wei *et al.*, 2014; Fig. 11c and d). In Pb–Pb isotope space (Fig. 11c and d),  $^{207}Pb/^{204}Pb_i$  and  $^{208}Pb/^{204}Pb_i$  of the plagioclase separates correlate positively with  $^{206}Pb/^{204}Pb_i$  and plot well above the Northern Hemisphere Reference Line (Hart, 1984).

Initial  $^{87}Sr/^{86}Sr$  and  $\epsilon Nd$  values of the crosscutting dykes range from 0.7034 to 0.7057 and from –3.7 to 4.8, respectively. Sample 4202-16 is distinct from the other samples in having the highest  $^{87}Sr/^{86}Sr_i$  (0.7057) and lowest  $\epsilon Nd_i$  (–3.7) (Table 3, Fig. 11a). Except for sample 4202-16, the dykes have lower  $^{87}Sr/^{86}Sr_i$  and higher  $\epsilon Nd_i$  than the wehrlites. They also exhibit similar  $\epsilon Nd_i$  to the least contaminated dykes intruding the Carboniferous–early Permian sedimentary sequence in the Xiaohaizi area (Zhou *et al.*, 2009; Wei *et al.*, 2014), but have apparently higher  $\epsilon Nd_i$  than the Keping basalts (Fig. 11a; Zhou *et al.*, 2009; Zhang *et al.*, 2010a; Yu *et al.*, 2011b; Li *et al.*, 2012b; Wei *et al.*, 2014).

## DISCUSSION

### Rock types and age relations

One of the prominent features of the Xiaohaizi area is the presence of numerous dykes that crosscut the wehrlite and syenite. The crosscutting relationships suggest that the wehrlites were emplaced first, followed by the Xiaohaizi syenite, mafic dykes and quartz syenite porphyries. The ages of the Xiaohaizi wehrlites obtained in this study are essentially consistent with the SIMS U–Pb concordia age of  $279.7 \pm 2.0$  Ma ( $2\sigma$ ) for the Xiaohaizi syenite (Wei & Xu, 2011) and ages determined using other methods (277–282 Ma; Yang *et al.*, 2006; Li *et al.*, 2007; Zhang *et al.*, 2010a). Yu (2009) reported a sensitive high-resolution ion microprobe (SHRIMP) zircon U–Pb age of  $278.4 \pm 2.2$  Ma for a quartz syenite porphyry, which is indistinguishable from that of the syenite and the wehrlites. These ages suggest that diverse magmatic rocks in the Xiaohaizi area were essentially emplaced simultaneously.

Figure 12 shows a probability density plot for all the available ages from the Xiaohaizi and adjacent areas in the Tarim LIP. The Tarim LIP is characterized by two main episodes ( $\sim 289$  Ma and  $\sim 279$  Ma) of magmatism. The earlier episode is represented by voluminous flood basalts and rhyolites, formed at 286–292 Ma, and peaked at  $288.9 \pm 1.3$  Ma ( $2\sigma$ ; Fig. 12). The later episode is marked by ultramafic–mafic–felsic intrusions, rhyolites, and numerous mafic and felsic dykes in the Bachu and Piquang areas (Fig. 1). These rocks were emplaced between 272 and 284 Ma, with the main pulse at 277–284 Ma peaking at  $278.6 \pm 1.2$  Ma ( $2\sigma$ ; Fig. 12). The age of the Xiaohaizi wehrlite intrusion, combined with its genetic relationships to the Bachu dykes and syenites (see discussion below), suggests that it is an important part of the second stage of the Tarim LIP.

Table 2: Whole-rock major and trace element data.

Cumulate wehrlites														
Sample:	4202-13 <sup>1</sup>	4202-14	4202-18	4202-24	4202-27	4202-30	4202-33	4202-39	4202-41 <sup>1</sup>	4202-43 <sup>1</sup>	4202-47	4202-49	4202-51 <sup>1</sup>	4202-52 <sup>1</sup>
<i>Major elements (wt %)</i>														
SiO <sub>2</sub>	36.83	36.45	37.15	37.81	36.33	37.07	37.93	37.61	38.53	37.95	38.54	38.83	38.26	37.81
TiO <sub>2</sub>	3.12	3.15	3.15	3.03	3.08	3.16	2.51	3.54	2.30	2.77	2.85	2.31	2.44	3.49
Al <sub>2</sub> O <sub>3</sub>	5.29	5.14	5.14	5.92	5.50	5.15	3.69	9.98	4.91	5.54	5.03	5.43	3.61	5.53
Fe <sub>2</sub> O <sub>3</sub> T	25.34	24.84	25.02	24.41	24.13	24.91	24.30	22.13	22.72	23.65	23.06	22.90	22.98	22.76
MnO	0.23	0.22	0.22	0.22	0.22	0.23	0.24	0.16	0.21	0.22	0.22	0.23	0.23	0.23
MgO	20.07	19.15	19.54	18.71	18.83	19.89	22.52	13.55	22.00	20.25	19.87	21.70	22.63	20.66
CaO	8.90	8.68	9.40	9.53	9.23	9.56	8.58	12.49	9.33	9.61	9.96	8.09	8.76	8.98
Na <sub>2</sub> O	0.36	0.34	0.40	0.54	0.34	0.32	0.29	0.58	0.32	0.36	0.41	0.59	0.43	0.45
K <sub>2</sub> O	0.02	0.34	0.06	0.06	0.16	0.02	0.05	0.03	0.02	0.03	0.10	0.14	0.11	0.15
P <sub>2</sub> O <sub>5</sub>	0.01	0.01	0.02	0.03	0.01	0.01	0.02	0.01	0.01	0.02	0.02	0.11	0.02	0.01
LOI	-0.74	1.36	-0.65	-0.80	1.59	-0.87	-0.68	-0.60	-0.88	-0.94	-0.59	-0.85	-0.02	-0.60
Total	99.4	99.4	99.4	99.5	99.4	99.4	99.4	99.5	99.5	99.5	99.5	99.5	99.4	99.5
Mg#	61	60	61	60	61	61	65	55	66	63	63	65	66	64
<i>Trace elements (ppm)</i>														
Sc	36.2	35.1	40.3	37.6	37.9	39.3	39.8	41.9	38.8	39.1	42.0	31.4	40.2	35.4
V	505	372	383	359	391	380	404	548	336	471	355	331	300	422
Cr	753	539	587	551	615	597	1147	456	1056	837	727	649	1201	1026
Co	179	138	164	165	143	156	172	124	163	160	147	161	158	154
Ni	589	483	566	533	503	535	648	633	723	677	537	601	684	626
Cu	197	170	275	224	161	182	168	305	139	146	204	154	73.8	57.3
Zn	161	149	161	162	182	160	167	146	137	151	153	153	166	160
Ga	13.8	12.8	13.3	14.1	13.2	12.9	10.7	17.4	11.3	13.5	12.5	11.4	10.7	12.3
Rb	0.46	1.61	1.50	1.10	6.43	0.62	1.31	0.40	0.37	0.49	2.77	2.71	2.40	3.95
Sr	190	197	226	231	229	222	127	342	171	200	224	226	111	214
Y	6.02	6.15	6.63	7.26	5.82	6.19	6.79	6.52	5.94	6.41	7.46	8.89	7.04	5.87
Zr	28.6	33.3	32.7	39.4	25.6	26.8	34.3	27.7	24.0	27.9	46.8	41.1	33.2	30.7
Nb	2.45	2.60	2.95	4.37	1.76	1.94	3.53	2.00	1.60	2.22	4.14	6.11	3.42	5.18
Cs	0.01	0.05	0.05	0.04	0.23	0.03	0.03	0.01	0.01	0.01	0.08	0.06	0.10	0.18
Ba	34.6	69.5	64.2	76.5	63.2	43.6	40.4	52.4	24.3	33.1	80.5	136	48.4	57.3
La	2.39	2.85	2.73	3.92	2.01	2.02	2.96	2.50	1.80	2.26	3.84	7.53	4.78	2.21
Ce	6.58	7.53	7.56	10.09	5.87	6.15	8.66	7.36	5.45	6.47	10.10	18.51	11.01	6.07
Pr	1.08	1.22	1.28	1.57	1.03	1.10	1.36	1.20	0.96	1.10	1.59	2.70	1.54	1.01
Nd	5.59	6.44	6.57	7.91	5.63	5.97	7.04	6.29	5.14	5.81	7.94	12.34	7.15	5.26
Sm	1.64	1.77	1.82	2.06	1.62	1.75	1.88	1.81	1.58	1.72	2.14	2.80	1.91	1.54
Eu	0.63	0.68	0.66	0.78	0.62	0.65	0.67	0.74	0.61	0.68	0.78	0.94	0.80	0.64
Gd	1.78	1.79	1.82	2.05	1.68	1.76	1.93	1.85	1.76	1.87	2.09	2.66	2.07	1.70
Tb	0.26	0.29	0.30	0.34	0.26	0.29	0.32	0.29	0.26	0.28	0.33	0.41	0.30	0.25
Dy	1.43	1.54	1.60	1.77	1.45	1.49	1.58	1.52	1.40	1.54	1.78	2.21	1.65	1.37
Ho	0.26	0.28	0.28	0.32	0.25	0.28	0.29	0.27	0.25	0.28	0.33	0.39	0.30	0.25
Er	0.61	0.67	0.68	0.76	0.58	0.66	0.69	0.63	0.60	0.65	0.78	0.94	0.71	0.60
Tm	0.08	0.08	0.08	0.10	0.08	0.08	0.09	0.08	0.08	0.08	0.10	0.12	0.09	0.08
Yb	0.45	0.50	0.49	0.57	0.43	0.48	0.50	0.46	0.44	0.47	0.58	0.70	0.53	0.45
Lu	0.06	0.07	0.07	0.08	0.07	0.07	0.08	0.06	0.06	0.06	0.09	0.10	0.07	0.06

(continued)

Table 2: Continued

Cumulate wehrlites														
Sample:	4202-13 <sup>1</sup>	4202-14	4202-18	4202-24	4202-27	4202-30	4202-33	4202-39	4202-41 <sup>1</sup>	4202-43 <sup>1</sup>	4202-47	4202-49	4202-51 <sup>1</sup>	4202-52 <sup>1</sup>
Hf	1.06	1.23	1.14	1.32	1.00	1.11	1.30	1.19	1.00	1.10	1.55	1.41	1.21	1.12
Ta	0.27	0.24	0.30	0.42	0.18	0.24	0.32	0.24	0.18	0.22	0.38	0.47	0.29	0.44
Pb	0.99	0.83	0.87	0.66	2.43	0.87	1.12	1.08	0.33	1.67	1.55	1.36	5.32	1.77
Th	0.13	0.29	0.15	0.32	0.11	0.11	0.22	0.07	0.06	0.09	0.56	0.43	0.17	0.08
U	0.03	0.08	0.04	0.06	0.04	0.03	0.05	0.02	0.02	0.02	0.11	0.09	0.07	0.03
Eu/Eu*	1.12	1.15	1.09	1.14	1.14	1.12	1.06	1.22	1.11	1.15	1.11	1.03	1.22	1.20

Cumulate wehrlites										Dykes				
Sample:	4202-53 <sup>1</sup>	4202-55	4202-57 <sup>1</sup>	4202-58	4202-60	4202-61 <sup>1</sup>	4202-63	4202-64	XHZ-15 <sup>1</sup>	XHZ-16 <sup>1</sup>	4202-9 <sup>1</sup>	4202-16	4202-20 <sup>1</sup>	4202-45 <sup>1</sup>
Major elements (wt %)														
SiO <sub>2</sub>	39.68	38.78	40.57	39.11	39.84	39.23	41.68	39.25			51.04	52.39	56.25	50.35
TiO <sub>2</sub>	3.85	2.04	2.04	1.73	1.75	1.83	1.73	1.94			2.62	2.48	1.68	2.94
Al <sub>2</sub> O <sub>3</sub>	6.30	4.56	3.69	4.36	4.99	4.09	5.45	4.47			14.27	14.02	16.41	14.28
Fe <sub>2</sub> O <sub>3</sub> T	20.49	22.66	20.12	22.08	20.80	21.74	19.42	22.04			12.36	10.72	8.55	11.99
MnO	0.22	0.24	0.21	0.23	0.21	0.22	0.20	0.22			0.15	0.13	0.14	0.18
MgO	18.81	23.63	22.57	24.44	23.29	24.32	21.55	23.36			3.60	2.94	2.35	3.81
CaO	10.12	8.04	10.45	8.06	8.77	8.09	8.04	8.34			7.74	6.52	5.06	7.60
Na <sub>2</sub> O	0.66	0.35	0.35	0.36	0.42	0.58	1.04	0.37			3.84	3.51	4.68	3.92
K <sub>2</sub> O	0.07	0.05	0.07	0.04	0.06	0.06	0.29	0.09			1.60	2.34	2.89	1.82
P <sub>2</sub> O <sub>5</sub>	0.03	0.01	0.02	0.02	0.02	0.02	0.03	0.02			0.91	0.51	0.67	0.87
LOI	-0.73	-0.87	-0.61	-0.93	-0.66	-0.69	0.07	-0.62			1.45	4.19	0.89	1.82
Total	99.50	99.47	99.48	99.49	99.48	99.49	99.50	99.47			99.57	99.76	99.55	99.58
Mg#	65	67	69	69	69	69	69	68			37	35	35	39
Trace elements (ppm)														
Sc	40.0	33.2	46.8	32.0	34.4	33.5		33.8	34.8	35.3	14.6	16.1	12.1	15.3
V	307	324	262	278	283	242		284	150	247	81	132	42	115
Cr	880	813	1430	939	994	1255		1203	845	837	0.16	3.81	0.44	0.06
Co	146	162	153	162	155	172		166	132	121	34.7	57.5	12.9	19.4
Ni	596	708	731	750	695	826		721	795	865	4.38	5.11	2.68	0.89
Cu	132	105	59.6	68.0	74.5	93.0		112	25.2	194	135	67.8	37.3	74.8
Zn	140	147	136	136	126	144		149	120	127	98.0	104	101	93.5
Ga	12.4	9.70	9.51	8.88	9.48	9.21		9.31	6.13	9.71	26.1	23.1	28.4	25.9
Rb	1.08	1.34	1.73	0.79	1.36	1.24		2.40	9.42	10.5	29.7	35.9	54.5	22.1
Sr	273	223	116	220	233	153		159	158	197	862	614	818	918
Y	9.14	5.06	8.54	5.29	5.66	5.96		5.87	10.1	11.1	42.0	31.7	52.7	42.0
Zr	58.1	24.2	36.0	23.3	28.0	28.3		29.9	54.7	77.2	475	247	732	426
Nb	11.5	1.90	3.25	1.88	2.09	2.77		2.82	7.00	8.09	89.9	42.1	124	87.2
Cs	0.02	0.04	0.06	0.03	0.06	0.02		0.06	0.43	0.49	0.35	0.15	0.32	0.12
Ba	65.7	59.5	38.6	49.2	66.0	36.6		45.2	132	154	716	1128	969	697
La	4.59	1.97	3.09	2.23	2.65	2.55		2.95	8.00	9.70	79.3	48.0	114	68.1
Ce	11.95	5.56	8.95	6.06	6.92	6.75		8.00	19.2	22.9	168	97.7	250	155

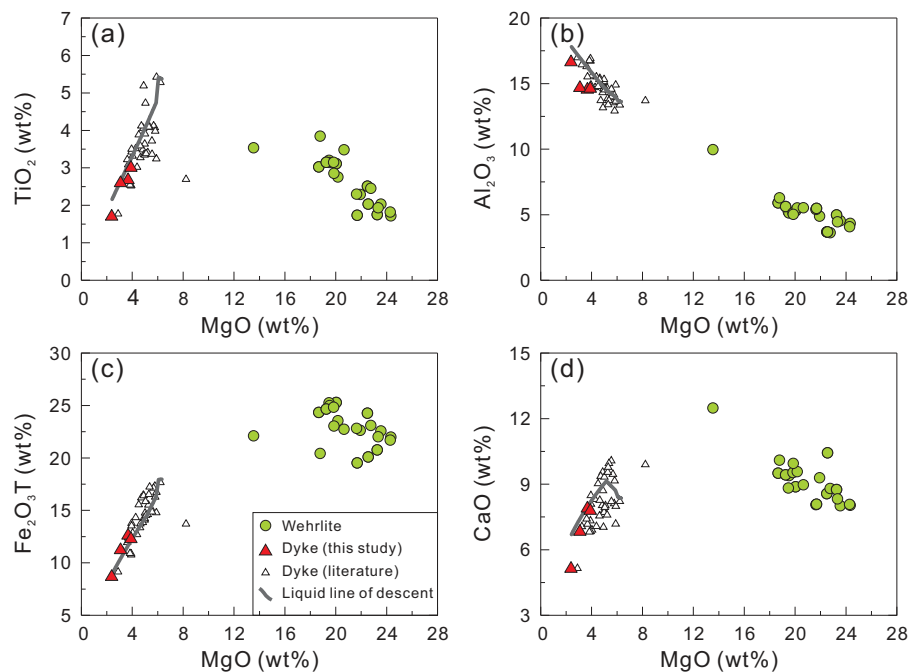
(continued)

Table 2: Continued

Sample:	Cumulate wehrlites										Dykes			
	4202-53 <sup>1</sup>	4202-55	4202-57 <sup>1</sup>	4202-58	4202-60	4202-61 <sup>1</sup>	4202-63	4202-64	XHZ-15 <sup>1</sup>	XHZ-16 <sup>1</sup>	4202-9 <sup>1</sup>	4202-16	4202-20 <sup>1</sup>	4202-45 <sup>1</sup>
Pr	1.85	0.91	1.50	1.02	1.12	1.09		1.19	2.80	3.24	18.8	12.3	27.8	17.8
Nd	8.98	4.86	7.74	5.19	5.65	5.45		6.00	13.2	14.7	73.2	49.9	107	71.6
Sm	2.46	1.37	2.24	1.40	1.52	1.56		1.63	3.20	3.48	14.3	9.72	19.6	14.4
Eu	0.95	0.53	0.80	0.55	0.60	0.60		0.61	1.00	1.09	4.51	3.13	5.71	4.49
Gd	2.59	1.38	2.45	1.47	1.59	1.70		1.63	3.04	3.48	12.55	8.73	15.91	12.74
Tb	0.39	0.23	0.36	0.24	0.26	0.25		0.26	0.48	0.54	1.75	1.30	2.24	1.80
Dy	2.13	1.18	1.99	1.29	1.36	1.39		1.34	2.51	2.81	9.26	6.80	11.7	9.44
Ho	0.39	0.22	0.36	0.23	0.25	0.25		0.26	0.44	0.49	1.68	1.24	2.12	1.70
Er	0.92	0.50	0.85	0.55	0.60	0.61		0.61	1.06	1.17	4.17	3.19	5.37	4.22
Tm	0.12	0.06	0.11	0.07	0.07	0.08		0.08	0.13	0.15	0.51	0.42	0.67	0.52
Yb	0.70	0.39	0.63	0.41	0.44	0.46		0.45	0.77	0.88	3.09	2.63	4.04	3.05
Lu	0.10	0.06	0.09	0.06	0.07	0.06		0.07	0.11	0.12	0.43	0.39	0.56	0.42
Hf	1.83	0.92	1.37	0.86	1.03	1.02		1.11	1.67	2.38	10.54	8.29	15.8	9.28
Ta	0.86	0.22	0.29	0.20	0.25	0.26		0.31	0.56	0.64	5.17	2.95	6.98	5.00
Pb	0.55	0.31	1.01	0.08	0.76	0.56		0.84	1.97	3.30	5.11	6.49	6.63	8.55
Th	0.31	0.17	0.20	0.16	0.26	0.24		0.43	0.92	1.61	7.28	8.50	12.6	7.11
U	0.07	0.03	0.05	0.04	0.06	0.06		0.09	0.26	0.43	1.97	1.80	3.39	1.86
Eu/Eu*	1.14	1.16	1.04	1.16	1.17	1.12		1.13	0.96	0.95	1.00	1.02	0.96	0.99

Mg# = 100 Mg/(Mg + Fe<sup>2+</sup>); LOI, loss on ignition.

<sup>1</sup>Samples analyzed at UQ; the others were analyzed at GIG-CAS.



**Fig. 8.** Variation of selected major oxides vs MgO for the Xiaohaizi cumulate wehrlites and dykes. Also plotted for comparison are data for dykes intruding the sedimentary strata around the Xiaohaizi syenite complex. Fractional crystallization was modeled for the dykes using MELTS (Ghiorso & Sack, 1995) at 0.2 GPa for a moderately hydrous magma composition (0.8 wt % H<sub>2</sub>O in starting magma), with oxygen fugacity at the quartz–fayalite–magnetite (QFM) buffer. Sample 08KT18-9 (Zhang *et al.*, 2010a) was chosen as the starting magma composition as this sample had relatively higher MgO, TiO<sub>2</sub> and Fe<sub>2</sub>O<sub>3</sub>T contents. Data sources: dykes (literature) from Zhou *et al.* (2009), Zhang *et al.* (2010a) and Wei *et al.* (2014).



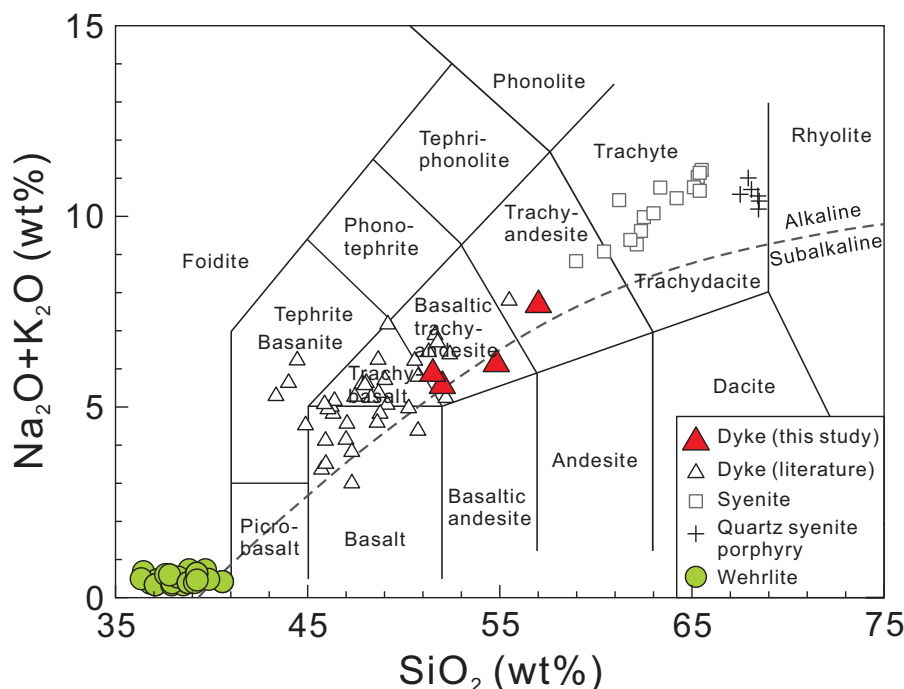


**Fig. 9.** (a) Total alkalis ( $\text{Na}_2\text{O} + \text{K}_2\text{O}$ ) vs  $\text{SiO}_2$  (TAS; Le Bas *et al.*, 1986). The alkaline–subalkaline divide is from Irvine & Baragar (1971). It should be noted that the wehrlites are plotted on the diagram only for comparison rather than classification. Data sources as in Fig. 8; syenites from Sun *et al.* (2008) and Wei & Xu (2011); quartz syenite porphyries from Yang *et al.* (2007) and Yu (2009).

### Formation of the crosscutting dyke magmas through closed-system fractional crystallization

The positive correlations between  $\text{TiO}_2$ ,  $\text{Fe}_2\text{O}_3\text{T}$ ,  $\text{CaO}$  and  $\text{MgO}$  (Fig. 8) for the dyke are consistent with olivine, clinopyroxene and Fe–Ti oxide fractionation. This is supported by the apparently low Ni and Cr contents.  $\text{Al}_2\text{O}_3$  correlates negatively with  $\text{MgO}$  (Fig. 8), arguing against significant plagioclase fractionation. The potential effects of closed-system magmatic differentiation in a magma chamber can be evaluated by calculating a liquid line of descent (Fig. 8) using MELTS (Ghiorso & Sack, 1995), assuming upper-crustal pressures, moderately oxidizing conditions and moderate water contents. Low-pressure fractional crystallization of olivine + magnetite followed by clinopyroxene + magnetite assemblages yields a liquid line of descent that is consistent with the major element variations displayed by the dykes (Fig. 8). The more evolved dykes could be formed by 36% fractional crystallization from a magma with the same composition as sample 08KT18-9 with relatively higher  $\text{MgO}$ ,  $\text{TiO}_2$  and  $\text{Fe}_2\text{O}_3\text{T}$  contents [starting composition data from Zhang *et al.* (2010a)].

The dykes (except for sample 4202-16) show enrichment in Nb–Ta (Fig. 10b) and have relatively high Nb/U (36.5–46.8), Ce/Pb (18.2–37.8) and Nb/La (1.08–1.28) ratios similar to OIB (Hofmann, 2003); they also have low

( $^{87}\text{Sr}/^{86}\text{Sr}$ )<sub>i</sub> (0.70337–0.70345) and high  $\epsilon\text{Nd}_i$  (4.3–4.8) (Fig. 11a). Similar compositions have also been observed for mafic dykes intruding the Carboniferous–early Permian sedimentary sequence in the Xiaohaizi area (Zhou *et al.*, 2009; Zhang *et al.*, 2010a; Wei *et al.*, 2014) (Figs 8 and 10a, b), suggesting a similar emplacement age. It seems that they were not affected by crustal contamination and that their trace element and isotopic characteristics reflect those of their mantle source. The exception is sample 4202-16, which may have experienced crustal contamination given its low Nb/U (23.4), Ce/Pb (15.1) and Nb/La (0.88) ratios, high ( $^{87}\text{Sr}/^{86}\text{Sr}$ )<sub>i</sub> (0.70568) and negative  $\epsilon\text{Nd}_i$  (–3.7).

The dykes exhibit higher  $\epsilon\text{Nd}_i$  than the Keping basalts ( $\epsilon\text{Nd}_i = -2$  to  $-4$ ), which have been proposed to be derived from a long-term enriched Tarim subcontinental lithospheric mantle (SCLM) source (Zhou *et al.*, 2009; Zhang *et al.*, 2010a; Li *et al.*, 2012b; Wei *et al.*, 2014). This implies that the dykes cannot be derived from the Tarim SCLM source. The uncontaminated dykes exhibit incompatible trace element patterns (Fig. 10) and ratios (e.g. Nb/Zr, La/Nb) strikingly similar to those of OIB and the least contaminated Emeishan high-Ti basalts, but are distinct from mid-ocean ridge basalt (MORB; Fig. 13). They also have trace element ratios (e.g. Nb/La = 1.08–1.28) and Nd isotope compositions ( $\epsilon\text{Nd}_i = 4.3$ – $4.8$ ) similar to the proposed plume component (Nb/La = 1.0–1.1,

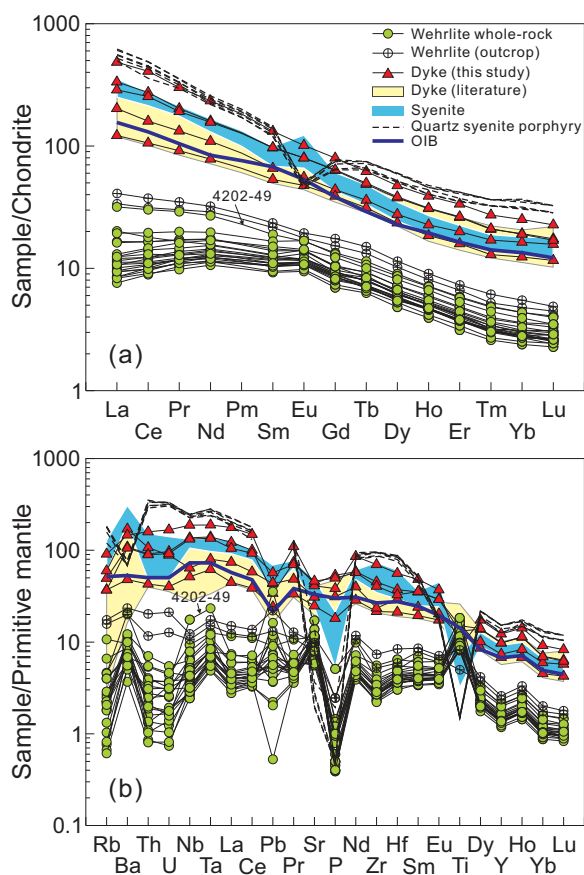


**Fig. 10.** Chondrite-normalized REE patterns (a) and primitive mantle-normalized multi-element patterns (b) for the Xiaohaizi cumulate wehrlites and dykes. Also shown for comparison are data for dykes intruding the sedimentary strata around the Xiaohaizi syenite complex and a typical ocean island basalt (OIB) from Sun & McDonough (1989). Chondrite and primitive mantle normalization values are from McDonough & Sun (1995). Data sources as in Figs 8 and 9.

$\epsilon\text{Nd}_i = 4.6\text{--}4.8$ ) for the Emeishan high-Ti basalts (Xu *et al.*, 2001). These features suggest that the magmas that formed the dykes were probably derived from an enriched asthenospheric mantle source.

### Formation of the Xiaohaizi wehrlites through open-system fractionation

#### *Estimates of pressure, temperature and oxygen fugacity*

Establishing the pressure and temperature of formation of the wehrlites is difficult as the mineral assemblages are not compatible with many established thermobarometers. The syenite, which intruded the Xiaohaizi wehrlites, is therefore used to constrain the upper limit of the crystallization pressure for the wehrlites. This pressure is estimated using the Al-in-hornblende thermobarometer (Anderson & Smith, 1995) for the Xiaohaizi syenite and

ranges between 1.6 and  $2.1 \pm 0.6$  kbar (Supplementary Dataset 9). The clinopyroxenes of the Xiaohaizi wehrlites have low Na and Al contents and  $\text{Al}^{\text{VI}}/\text{Al}^{\text{IV}}$  ratios, indicating that they probably crystallized at low pressures, as high Na, Al and  $\text{Al}^{\text{VI}}/\text{Al}^{\text{IV}}$  are characteristic of clinopyroxenes crystallized at high pressures (Wass, 1979; Dobosi & Fodor, 1992; Haase *et al.*, 1996).

Application of the magnetite–ilmenite thermometer and oxygen barometer [using the ILMAT software of Lepage (2003)] to the magnetite–ilmenite pairs included in clinopyroxene yields temperatures ranging between 609 and 698°C, with one pair yielding a significantly higher temperature of 814°C (Fig. 14; Supplementary Dataset 10). Oxygen fugacities calculated from these mineral pairs are high to very high, ranging from FMQ – 1.6 to FMQ – 0.2, where FMQ is the fayalite–magnetite–quartz buffer. The calculated temperatures and oxygen fugacities for the interstitial magnetite–ilmenite pairs range from 571 to 762°C and from FMQ – 2.5 to FMQ + 1.4, respectively. The temperatures obtained range between 571 and 814°C; even if these were co-precipitating phases they probably reflect significant subsolidus re-equilibration.

### Liquid line of descent

The petrography of the wehrlites suggests that olivine and clinopyroxene are cumulus phases, whereas the Fe–Ti oxides (magnetite and ilmenite) and plagioclase are interstitial between olivine and clinopyroxene. This suggests later crystallization of plagioclase and Fe–Ti oxides compared with cumulus olivine and clinopyroxene. In addition, smaller plagioclase and Fe–Ti oxide grains occur as inclusions in some clinopyroxenes, indicating that they crystallized simultaneously. The sequential crystallization of minerals can also be determined using a geochemical approach.

At higher Mg# ( $> \sim 78$ ), the increasing  $\text{TiO}_2$  contents in clinopyroxenes with decreasing Mg# (Fig. 5a) follows a normal mafic mineral (olivine + clinopyroxene) fractionation trend, arguing against significant Fe–Ti oxide fractionation. At Mg#  $< \sim 78$ , however, with decreasing Mg#,  $\text{TiO}_2$  does not display any significant variation (Fig. 5a). This can be attributed to Fe–Ti oxide fractionation by which the increase of  $\text{TiO}_2$  caused by olivine and clinopyroxene fractionation is compromised. In addition, chromium is highly incompatible in plagioclase ( $D_{\text{Cr}}^{\text{Plag/Liq}} = 0.02\text{--}0.11$ ; Bindeman *et al.*, 1998; Aigner-Torres *et al.*, 2007), slightly incompatible to compatible in olivine ( $D_{\text{Cr}}^{\text{Ol/Liq}} = 0.6\text{--}1.9$ ; Beattie, 1994), compatible in clinopyroxene ( $D_{\text{Cr}}^{\text{Cpx/Liq}} = 3.8$ ; Hart & Dunn, 1993), and highly compatible in Fe–Ti oxides ( $D_{\text{Cr}}^{\text{Mt/Liq}} = 50\text{--}230$ ;  $D_{\text{Cr}}^{\text{Ilm/Liq}} = 11\text{--}43$ ; Leeman *et al.*, 1978; Klemme *et al.*, 2006). Fractionation of Fe–Ti oxides, therefore, will leave the residual liquid strongly depleted in Cr; thus, clinopyroxene crystallizing from this resultant liquid will have a low Cr content. In the Xiaohaizi case, clinopyroxenes with higher Mg# ( $> \sim 78$ ) are relatively rich in  $\text{Cr}_2\text{O}_3$  (up to

Table 3: *Sr-Nd isotopes for the whole-rocks, clinopyroxene and plagioclase separates of the Xiaohaizi cumulate wehrlites and crosscutting dykes*

Sample	Rb	Sr	$^{87}\text{Rb}/^{86}\text{Sr}$	$^{87}\text{Sr}/^{86}\text{Sr}$	$\pm 2\sigma$	$^{87}\text{Sr}/^{86}\text{Sr}_i$	$\pm 2\sigma^1$	Sm	Nd	$^{147}\text{Sm}/^{144}\text{Nd}$	$^{143}\text{Nd}/^{144}\text{Nd}$	$\pm 2\sigma$	$^{143}\text{Nd}/^{144}\text{Nd}_i$	$\pm 2\sigma^2$	$\varepsilon_{\text{Nd}_i}^3$	$\pm 2\sigma$
<i>Cumulate wehrlites</i>																
4202-13 WR	0.46	190	0.0070	0.704286	0.000007	0.704258	0.000007	1.64	5.59	0.1769	0.512556	0.000009	0.512332	0.000013	1.06	0.25
4202-14 Cpx	0.39	64.2	0.0177	0.703991	0.000007	0.703921	0.000007	3.99	12.7	0.1905	0.512696	0.000005	0.512347	0.000011	1.35	0.22
4202-18 Cpx	0.43	71.3	0.0172	0.704105	0.000008	0.704036	0.000009	4.48	14.3	0.1897	0.512689	0.000008	0.512342	0.000013	1.25	0.25
4202-19 Cpx	0.37	65.5	0.0163	0.703974	0.000007	0.703909	0.000007	3.69	11.7	0.1907	0.512696	0.000008	0.512347	0.000013	1.35	0.25
4202-24 Cpx	0.38	70.2	0.0158	0.704079	0.000018	0.704016	0.000018	4.72	15.2	0.1878	0.512683	0.000005	0.512339	0.000011	1.21	0.21
4202-30 Cpx	0.41	68.2	0.0174	0.704090	0.000007	0.704020	0.000008	4.42	14.0	0.1905	0.512684	0.000005	0.512335	0.000011	1.12	0.22
4202-30 Pl	1.22	1395	0.0025	0.704323	0.000010	0.704312	0.000010	0.27	2.18	0.0760	0.512448	0.000007	0.512309	0.000010	0.61	0.20
4202-33 Cpx	0.65	69.0	0.0271	0.704013	0.000007	0.703905	0.000009	4.47	14.4	0.1875	0.512702	0.000005	0.512358	0.000011	1.57	0.21
4202-41 Cpx	0.58	67.9	0.0247	0.704024	0.000007	0.703926	0.000009	3.88	12.3	0.1900	0.512702	0.000006	0.512354	0.000012	1.48	0.22
4202-41 Pl	0.26	1431	0.0005	0.704293	0.000007	0.704291	0.000007	0.26	2.07	0.0754	0.512442	0.000008	0.512303	0.000011	0.51	0.21
4202-41 WR	0.37	171	0.0062	0.704300	0.000008	0.704276	0.000008	1.58	5.14	0.1853	0.512670	0.000006	0.512331	0.000011	1.04	0.22
4202-43 Cpx	0.46	70.7	0.0190	0.704028	0.000007	0.703952	0.000008	4.44	14.0	0.1922	0.512690	0.000007	0.512337	0.000012	1.17	0.24
4202-43 WR	0.49	200	0.0071	0.704285	0.000008	0.704257	0.000008	1.72	5.81	0.1792	0.512659	0.000007	0.512331	0.000012	1.04	0.23
4202-47 Cpx	0.56	68.6	0.0238	0.704018	0.000008	0.703923	0.000010	3.03	10.2	0.1800	0.512695	0.000006	0.512365	0.000011	1.70	0.22
4202-49 Cpx	0.48	66.7	0.0210	0.704011	0.000007	0.703928	0.000008	4.23	13.4	0.1905	0.512698	0.000006	0.512349	0.000012	1.40	0.23
4202-51 Cpx	0.72	69.0	0.0303	0.704127	0.000007	0.704006	0.000010	4.55	14.6	0.1888	0.512681	0.000008	0.512335	0.000013	1.13	0.25
4202-51 Pl	0.33	1516	0.0007	0.704274	0.000008	0.704271	0.000008	0.31	2.69	0.0686	0.512456	0.000005	0.512330	0.000008	1.03	0.16
4202-52 Cpx	0.46	70.1	0.0188	0.704107	0.000007	0.704032	0.000008	4.35	13.8	0.1910	0.512678	0.000006	0.512328	0.000012	0.99	0.23
4202-52 Cpx*	0.43	71.4	0.0173	0.704116	0.000007	0.704047	0.000008	4.50	14.2	0.1910	0.512674	0.000006	0.512324	0.000012	0.91	0.23
4202-52 Pl	1.67	1393	0.0032	0.704339	0.000007	0.704326	0.000007	0.26	2.20	0.0709	0.512425	0.000008	0.512295	0.000009	0.35	0.21
4202-52 WR	3.95	214	0.0532	0.704527	0.000008	0.704314	0.000014	1.54	5.26	0.1771	0.512643	0.000005	0.512318	0.000010	0.80	0.20
4202-53 WR	1.08	273	0.0114	0.704288	0.000008	0.704243	0.000008	2.46	8.98	0.1655	0.512633	0.000005	0.512330	0.000010	1.03	0.19
4202-57 WR	1.73	116	0.0431	0.704438	0.000008	0.704267	0.000012	2.24	7.74	0.1747	0.512648	0.000004	0.512327	0.000010	0.98	0.19
4202-58 Cpx	1.15	72.1	0.0463	0.704089	0.000007	0.703904	0.000012	4.29	13.9	0.1867	0.512684	0.000007	0.512342	0.000012	1.27	0.23
4202-58 Pl	0.11	1503	0.0002	0.704296	0.000006	0.704295	0.000006	0.29	2.67	0.0655	0.512431	0.000007	0.512311	0.000008	0.65	0.19
4202-61 Cpx	1.10	72.0	0.0443	0.703942	0.000007	0.703766	0.000012	3.24	10.6	0.1852	0.512712	0.000006	0.512372	0.000011	1.85	0.22
4202-61 Pl	0.32	1525	0.0006	0.704287	0.000008	0.704284	0.000008	0.32	2.92	0.0664	0.512445	0.000006	0.512323	0.000007	0.90	0.17
4202-61 WR	1.24	153	0.0235	0.704360	0.000007	0.704266	0.000009	1.56	5.45	0.1729	0.512645	0.000006	0.512328	0.000011	0.99	0.21
4202-64 Cpx	0.24	74.3	0.0093	0.704089	0.000007	0.704052	0.000007	4.36	13.9	0.1901	0.512690	0.000008	0.512342	0.000013	1.26	0.25
<i>Dykes</i>																
4202-9 WR	29.7	862	0.0998	0.703843	0.000010	0.703445	0.000024	14.3	73.2	0.1179	0.512731	0.000006	0.512515	0.000009	4.63	0.17
4202-16 WR	35.9	614	0.1690	0.706351	0.000007	0.705678	0.000037	9.72	49.9	0.1177	0.512301	0.000006	0.512086	0.000009	-3.75	0.17
4202-20 WR	54.5	818	0.1926	0.704141	0.000007	0.703374	0.000042	19.6	107	0.1107	0.512701	0.000007	0.512498	0.000009	4.31	0.18
4202-45 WR	22.1	918	0.0695	0.703686	0.000008	0.703409	0.000017	14.4	71.6	0.1217	0.512744	0.000008	0.512521	0.000010	4.75	0.20

<sup>1</sup>The quoted uncertainty in  $^{87}\text{Sr}/^{86}\text{Sr}_i$  is calculated by error propagation analysis using uncertainties of  $\pm 5\%$  for Rb and  $\pm 2\%$  for Sr.

<sup>2</sup>The quoted uncertainty in  $^{143}\text{Nd}/^{144}\text{Nd}_i$  is calculated by error propagation analysis using uncertainties of  $\pm 2\%$  for Sm and Nd for whole-rocks and clinopyroxene separates,  $\pm 5\%$  for Sm and  $\pm 2\%$  for Nd for plagioclase separates.

<sup>3</sup> $\varepsilon_{\text{Nd}_i}$  is calculated at 279 Ma using the present-day values for CHUR: ( $^{143}\text{Nd}/^{144}\text{Nd}$ )<sub>CHUR</sub> = 0.512638,  $^{147}\text{Sm}/^{144}\text{Nd}$  = 0.1967 (Jacobsen & Wasserburg, 1980).

\*Replicate analysis; WR, whole-rock; Cpx, clinopyroxene; Pl, plagioclase.

Table 4: Pb isotopes for plagioclase separates of the Xiaohaizi cumulate wehrlites

Sample	U	Th	Pb	<sup>208</sup> Pb/ <sup>204</sup> Pb	±2σ	<sup>232</sup> Th/ <sup>204</sup> Pb	<sup>207</sup> Pb/ <sup>204</sup> Pb	±2σ	<sup>235</sup> U/ <sup>204</sup> Pb	<sup>206</sup> Pb/ <sup>204</sup> Pb	±2σ	<sup>238</sup> U/ <sup>204</sup> Pb	<sup>208</sup> Pb/ <sup>204</sup> Pb <sub>i</sub>	±2σ <sup>1</sup>	<sup>207</sup> Pb/ <sup>204</sup> Pb <sub>i</sub>	±2σ <sup>1</sup>	<sup>206</sup> Pb/ <sup>204</sup> Pb <sub>i</sub>	±2σ <sup>1</sup>
4202-30 PI	0.03	0.11	4.28	37.873	0.005	1.706	15.477	0.002	0.003	17.531	0.002	0.442	37.849	0.005	15.476	0.002	17.511	0.020
4202-41 PI	0.01	0.04	1.63	37.845	0.004	1.430	15.482	0.001	0.003	17.561	0.002	0.362	37.825	0.004	15.481	0.001	17.545	0.016
4202-51 PI	0.01	0.04	2.73	37.905	0.004	1.045	15.512	0.001	0.002	17.652	0.002	0.294	37.890	0.004	15.511	0.001	17.639	0.013
4202-52 PI	0.01	0.03	1.53	37.829	0.003	1.285	15.474	0.001	0.002	17.470	0.001	0.320	37.811	0.003	15.473	0.001	17.456	0.014
4202-58 PI	0.01	0.03	2.05	37.921	0.004	1.094	15.492	0.002	0.002	17.637	0.001	0.324	37.905	0.004	15.491	0.002	17.623	0.014
4202-61 PI	0.03	0.09	2.71	37.983	0.003	2.053	15.497	0.001	0.004	17.718	0.001	0.619	37.955	0.004	15.496	0.002	17.690	0.027

<sup>1</sup>The quoted uncertainties in initial Pb isotopes are calculated by error propagation analysis using uncertainties of  $\pm 10\%$  for U,  $\pm 5\%$  for Th and  $\pm 3\%$  for Pb.

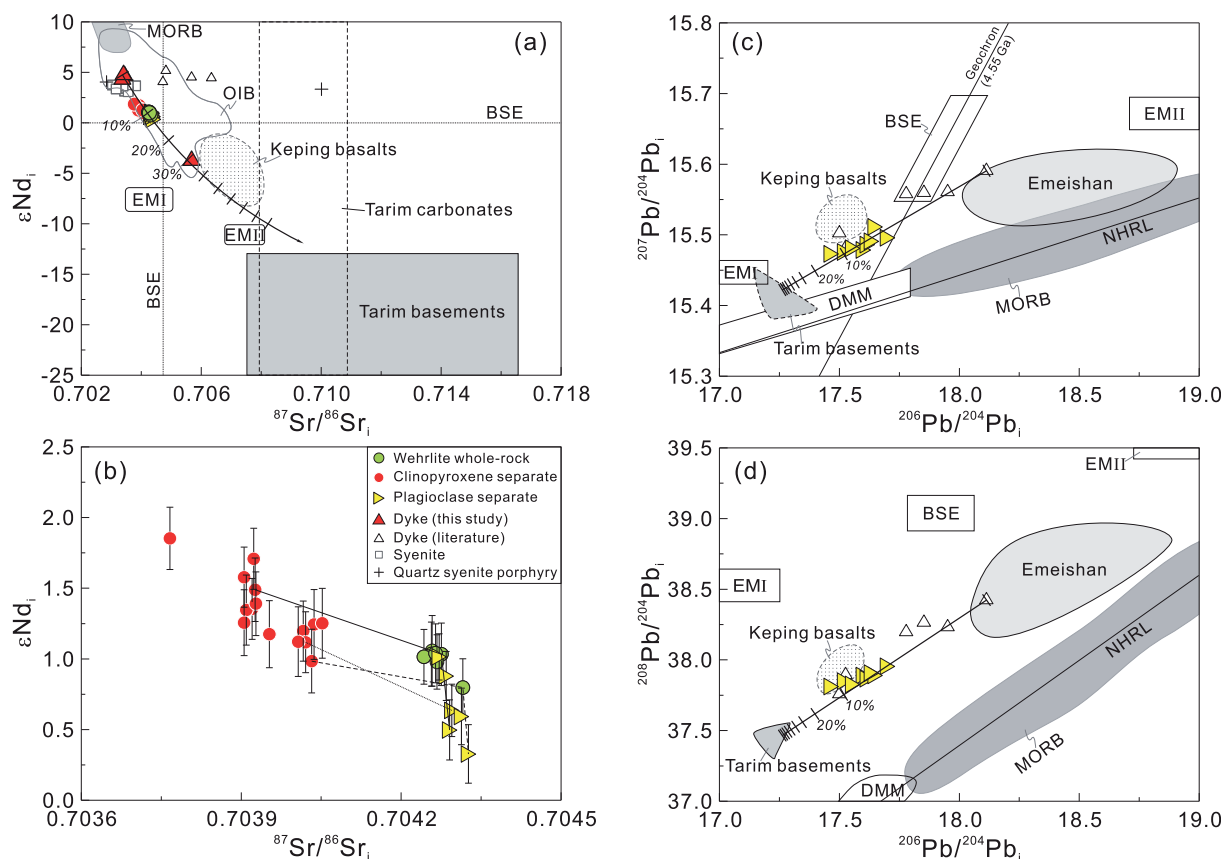


**Fig. 11.** (a) Initial Sr and Nd isotopic compositions of mineral separates and whole-rock samples of the Xiaohaizi cumulate wehrlites and dykes. The continuous line denotes a modeled AFC trend between a parental magma with trace element characteristics similar to those of an Emeishan high-Ti picrite (EM-79, Chung & Jahn, 1995) with 231 ppm Sr, 11.5 ppm Nd,  $^{87}\text{Sr}/^{86}\text{Sr}_i = 0.703374$  and  $\epsilon\text{Nd}_i = 4.75$  and a hybrid crustal contaminant of 30% carbonate and 70% Archean and Neoproterozoic basement with 374 ppm Sr, 27.6 ppm Nd,  $^{87}\text{Sr}/^{86}\text{Sr}_i = 0.7090$  and  $\epsilon\text{Nd}_i = -14.5$ ;  $K_D \text{ Sr} = 0.71$ ,  $K_D \text{ Nd} = 0.25$  (Bohrson & Spera, 2001),  $r = 0.5$ . (b) Enlargement of (a). Continuous and dashed lines connect a set of whole-rock, clinopyroxene and plagioclase analyses from samples 4202-41 and 4202-52, respectively; the dotted line connects a clinopyroxene–plagioclase pair from sample 4202-30. Error bars for  $\epsilon\text{Nd}_i$  are shown at the  $2\sigma$  level and for  $^{87}\text{Sr}/^{86}\text{Sr}_i$  the error bars are smaller than the symbols. (c, d) Initial Pb isotope compositions of plagioclase in the Xiaohaizi wehrlites and Bachu dykes. Continuous lines are modeled AFC trends with tick marks at 10% assimilation for a parental magma similar in isotope composition to a Bachu dyke (BC-2, Wei *et al.*, 2014) with 0.6 ppm Pb,  $^{206}\text{Pb}/^{204}\text{Pb}_i = 18.113$ ,  $^{207}\text{Pb}/^{204}\text{Pb}_i = 15.591$  and  $^{208}\text{Pb}/^{204}\text{Pb}_i = 38.424$ ;  $K_D \text{ Pb} = 0.17$  (Bohrson & Spera, 2001),  $r = 0.5$ . The crustal end-member utilized is similar to average Neoproterozoic basement with 12 ppm Pb,  $^{206}\text{Pb}/^{204}\text{Pb}_i = 17.226$ ,  $^{207}\text{Pb}/^{204}\text{Pb}_i = 15.415$  and  $^{208}\text{Pb}/^{204}\text{Pb}_i = 37.424$  (Cao *et al.*, 2011). Approximate locations of mantle end-members (Zindler & Hart, 1986) are indicated for reference. The Northern Hemisphere Reference Line (NHRL; Hart, 1984) is indicated. Also shown for comparison is a field for the Keping basalts (Zhou *et al.*, 2009; Zhang *et al.*, 2010a; Yu *et al.*, 2011b; Li *et al.*, 2012b; Wei *et al.*, 2014) and Emeishan least-contaminated high-Ti basalts (Zhang *et al.*, 2006). Data sources: Xiaohaizi syenites from Sun *et al.* (2008) and Wei & Xu, (2011); quartz syenite porphyries from Yu (2009); carbonate sediments from Shao *et al.* (2002), Zhu *et al.* (2002), He *et al.* (2004), Chen *et al.* (2010b) and Li *et al.* (2011a); Tarim Archean and Neoproterozoic basement from Zhang *et al.* (2007, 2012a), Long *et al.* (2010, 2011), Cao *et al.* (2011) and Ge *et al.*, (2012); dykes as in Fig. 8.



1.05 wt %, Fig. 5d; Supplementary Dataset 4), indicating that Fe–Ti oxide has not been largely separated from the liquid before the crystallization of high Mg# clinopyroxene (Mg# > 78). In contrast, Cr<sub>2</sub>O<sub>3</sub> contents in clinopyroxene with lower Mg# (< ~78) are relatively low (mostly falling within the range from the detection limit to 0.20 wt %) (Fig. 5d; Supplementary Dataset 4), suggesting significant crystallization of Fe–Ti oxides along with clinopyroxene. At higher Mg# values (> ~79), the fractionation of clinopyroxene must have been associated with negligible separation of plagioclase, given (1) the negative correlation between Al<sub>2</sub>O<sub>3</sub> content and Mg# of clinopyroxene (Fig. 5b), (2) the relatively high and

constant CaO content (23–24 %) without correlation with Mg# of clinopyroxene (Fig. 5c), and (3) plagioclase inclusions commonly occurring in clinopyroxenes with relatively low Mg# (< ~79) (Fig. 5e).

#### Parental magmas of the cumulate wehrlites and their genetic relationship with the dykes

The whole-rock Mg# of the cumulate wehrlites decreases and TiO<sub>2</sub> and Fe<sub>2</sub>O<sub>3</sub>T increase from the base of the core upwards (Fig. 6d–f), consistent with the stratigraphic variations of NiO in olivine and Cr<sub>2</sub>O<sub>3</sub> in magnetite (Fig. 6b and c). The Cr<sub>2</sub>O<sub>3</sub> content in magnetite decreases systematically from the base upwards. Chromium is slightly incompatible to compatible in olivine ( $D_{Cr}^{Ol/Liq} = 0.6–1.9$ ; Beattie, 1994), and compatible in clinopyroxene ( $D_{Cr}^{Cpx/Liq} = 3.8$ ; Hart & Dunn, 1993). Considering the mineral proportions of cumulus olivine (22–55%) and

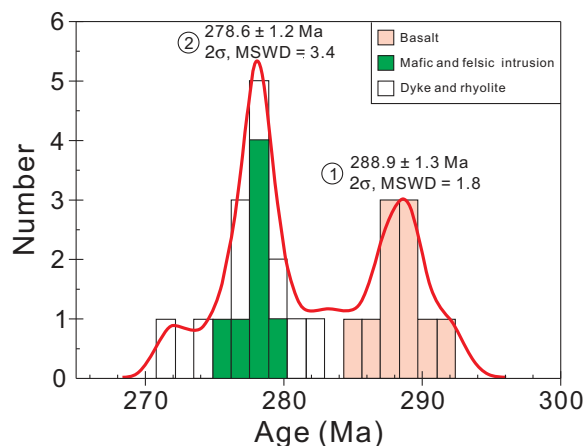


**Fig. 12.** Histogram and relative probability distribution of 25 dated basalts, mafic–felsic intrusions, mafic and felsic dykes and rhyolites from the Tarim LIP, showing two major peaks at ~279 and ~289 Ma. The numbers at the peaks of the probability curves (278.6 and 288.9 Ma) represent the weighted mean ages of both literature data and those reported in this study. Ages from conventional whole-rock <sup>40</sup>Ar/<sup>39</sup>Ar and U–Pb zircon data (Yang *et al.*, 1996, 2006; Li *et al.*, 2007, 2011b; Zhang *et al.*, 2008a, 2009, 2010a, 2012b; Yu, 2009; Tian *et al.*, 2010; Shanguan *et al.*, 2011; Wei & Xu, 2011; Yu *et al.*, 2011a, 2011b; Wei *et al.*, 2014 and this study).

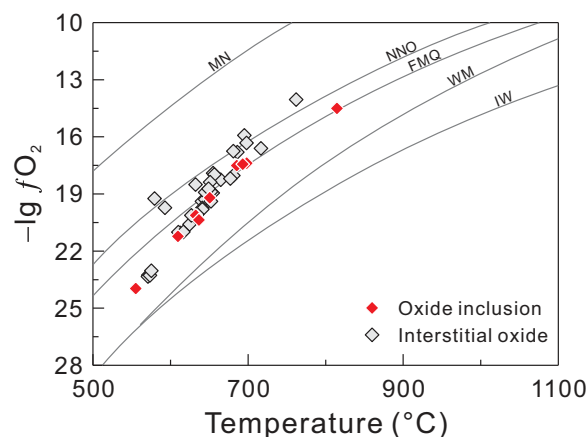


**Fig. 14.** Oxygen fugacity vs temperature calculated for the Xiaohaizi cumulate wehrlites based on magnetite–ilmenite equilibria. MN, magnetite–nickel buffer; NNO, nickel–nickel oxide; FMQ, fayalite–quartz–magnetite; WM, wüstite–magnetite; IW, iron–wüstite (Eugster & Wones, 1962).

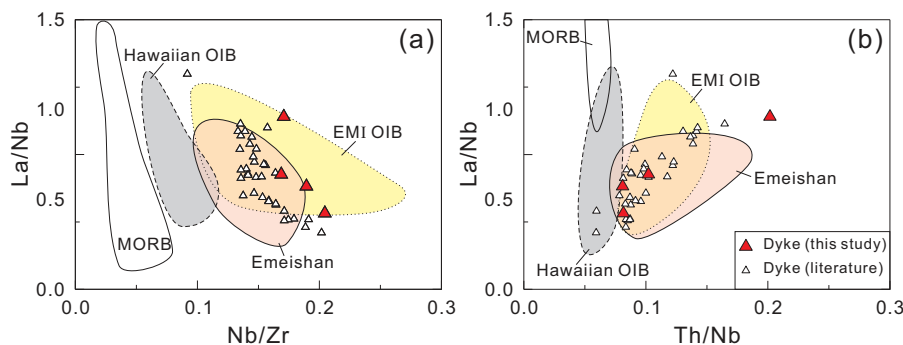


**Fig. 13.** Variation of La/Nb vs Nb/Zr (a) and Th/Nb (b) for the crosscutting dykes. For comparison fields are shown for enriched mantle type I (EMI) OIB (including Walvis Ridge, Gough and Tristan) from Willbold & Stracke (2006), Class & le Roex (2008) and Salters & Sachi-Kocher (2010); MORB from Salters & Stracke (2004); Hawaiian OIB from <http://georoc.mpch-mainz.gwdg.de/georoc/>; Emeishan least-contaminated high-Ti basalts from Xu *et al.* (2001), Xiao *et al.* (2004), Zhang *et al.* (2006) and Qi & Zhou (2008). Data sources for the dykes as in Fig. 8.

clinopyroxene (28–42%), Cr is overall compatible ( $D_{Cr} > 1$ ) in the cumulus assemblage. Therefore, the upward decrease in the Cr content of magnetite reflects a decrease in the Cr content of the residual liquid as a result of olivine and clinopyroxene fractionation. Magma chamber replenishment is common in large layered mafic intrusions, which will cause the cessation of magmatic differentiation and significant compositional reversals (e.g. Cawthorn *et al.*, 1991; Namur *et al.*, 2010). The lack of compositional reversals in the Xiaohaizi wehrlites from this interval suggests that they formed from a single magma pulse.

Major element variations can be ascribed to crystallization of cumulus phases from magmas evolving through fractional crystallization. For example, their high MgO, Cr and Ni (Table 2) contents reflect accumulation of olivine + clinopyroxene. Likewise, negative correlations between  $TiO_2$ ,  $Fe_2O_3$  and MgO (Fig. 8a and c), and the ubiquitous positive Eu anomaly in the wehrlite REE patterns (Fig. 10a) are consistent with variable amounts of interstitial Fe–Ti oxides and plagioclase. In addition, clinopyroxenes exhibit subparallel trace element patterns (Fig. 7) consistent with crystallization from similar parental melts. The low Mg# values of olivine and clinopyroxene (Supplementary Datasets 3 and 4) indicate that the wehrlites crystallized from a melt that had previously experienced fractional crystallization. The Mg# of the melts in equilibrium with the most primitive olivine (Fo = 75) and clinopyroxene rim (Mg# = 79), calculated using the partition coefficients for Fe and Mg between olivine or clinopyroxene and melt (Roeder & Emslie, 1970; Wood & Blundy, 1997) are 47 and 48, respectively. In addition, the calculated Mg# of the melt in equilibrium with the most primitive clinopyroxene core (Mg# = 84) is 57.

The calculated melts in equilibrium with the least evolved clinopyroxenes (Mg# > 80) have similar trace element patterns to the Emeishan high-Ti basalts (Fig. 7; Kamenetsky *et al.*, 2012), average OIB (Sun & McDonough, 1989) and the crosscutting dykes (Fig. 10). This suggests that the Xiaohaizi wehrlites were derived from melts with similar trace element compositions to the crosscutting dykes. However, the uncontaminated dykes have higher  $\epsilon Nd_i$  values than the wehrlites (Table 3; Fig. 11a). The Mg# value of the liquid in equilibrium with the cumulus olivine and clinopyroxene is ~48, which is significantly higher than that of the dykes (35–39). In addition, the isotopic differences between the cumulus clinopyroxene and intercumulus plagioclase in the Xiaohaizi wehrlite intrusion suggest that the extent of crustal contamination increases with magmatic differentiation (see discussion below). Therefore, the dykes and cumulate wehrlites cannot be derived from a common parental magma; rather they are more probably derived from different magma pulses in keeping with the field

relationships indicating that the dykes formed relatively later than the cumulate wehrlites.

#### *Assimilation and fractional crystallization (AFC) as a cause of isotopic disequilibrium*

Sr–Nd isotopic disequilibrium is evident between the clinopyroxene and plagioclase populations in the Xiaohaizi wehrlites. Within a single sample clinopyroxene mineral separates have lower  $^{87}Sr/^{86}Sr_i$  and higher  $\epsilon Nd_i$  than the whole-rocks and plagioclase separates (Table 3; Fig. 11b). The discrepancies between the Sr–Nd isotope compositions of the clinopyroxene and plagioclase separates are significantly greater than the analytical uncertainties calculated by error propagation (Table 3). In the Xiaohaizi wehrlites, olivine and clinopyroxene are cumulus phases, whereas plagioclase occurs interstitially between the silicates, thus representing trapped post-cumulus liquid. This suggests that clinopyroxene and plagioclase crystallized at different times from the same magma batch. Therefore, the initial isotope compositions of the clinopyroxene and plagioclase may be considered representative of those of magmas that had evolved to different stages; that is, earlier liquid crystallizing clinopyroxene and later interstitial liquid crystallizing plagioclase. Similar isotopic disequilibrium has also been observed for the Bushveld intrusion in South Africa and the Rum intrusion in Scotland and has been interpreted to reflect crystallization from magmas with different isotopic compositions (Mathez & Waight, 2003; Tepley & Davidson, 2003; Prevec *et al.*, 2005; Mathez & Kent, 2007; Chutas *et al.*, 2012; Roelofse & Ashwal, 2012; Yang *et al.*, 2013).

Higher  $^{87}Sr/^{86}Sr_i$  and lower  $\epsilon Nd_i$  values of plagioclase relative to clinopyroxene in the Xiaohaizi wehrlites could be explained by increasing degrees of crustal contamination during magmatic differentiation. Crustal contamination is supported by the positive correlation of  $^{87}Sr/^{86}Sr_i$  with the Zr/Nb ratio of the clinopyroxenes (Fig. 15a), and a negative correlation between  $\epsilon Nd_i$  and Zr/Nb (Fig. 15b). These compositional trends are similar to that expected for contamination of mantle-derived magmas by crustal contaminants (DePaolo, 1981; DePaolo & Wasserburg, 1979).

The upper crust in Tarim is dominated by Archean gneisses reworked during the Proterozoic and Neoproterozoic (Hu *et al.*, 2000; Cao *et al.*, 2011; Long *et al.*, 2011; Zhu *et al.*, 2011). The Archean and Neoproterozoic basement is characterized by high  $^{87}Sr/^{86}Sr_i$  (0.7075–0.7166) and low  $\epsilon Nd_i$  (–13 to –37, corrected to 279 Ma) (Fig. 11a). If the Tarim Archean basement and Neoproterozoic igneous rocks were the contaminants the earliest plagioclase formed during the AFC process would have a higher An content and reflect lower degrees of crustal contamination (i.e. lower  $^{87}Sr/^{86}Sr_i$  and higher  $\epsilon Nd_i$ ). As shown in Fig. 15c and d,  $^{87}Sr/^{86}Sr_i$  increases and  $\epsilon Nd_i$  decreases with increasing Ca

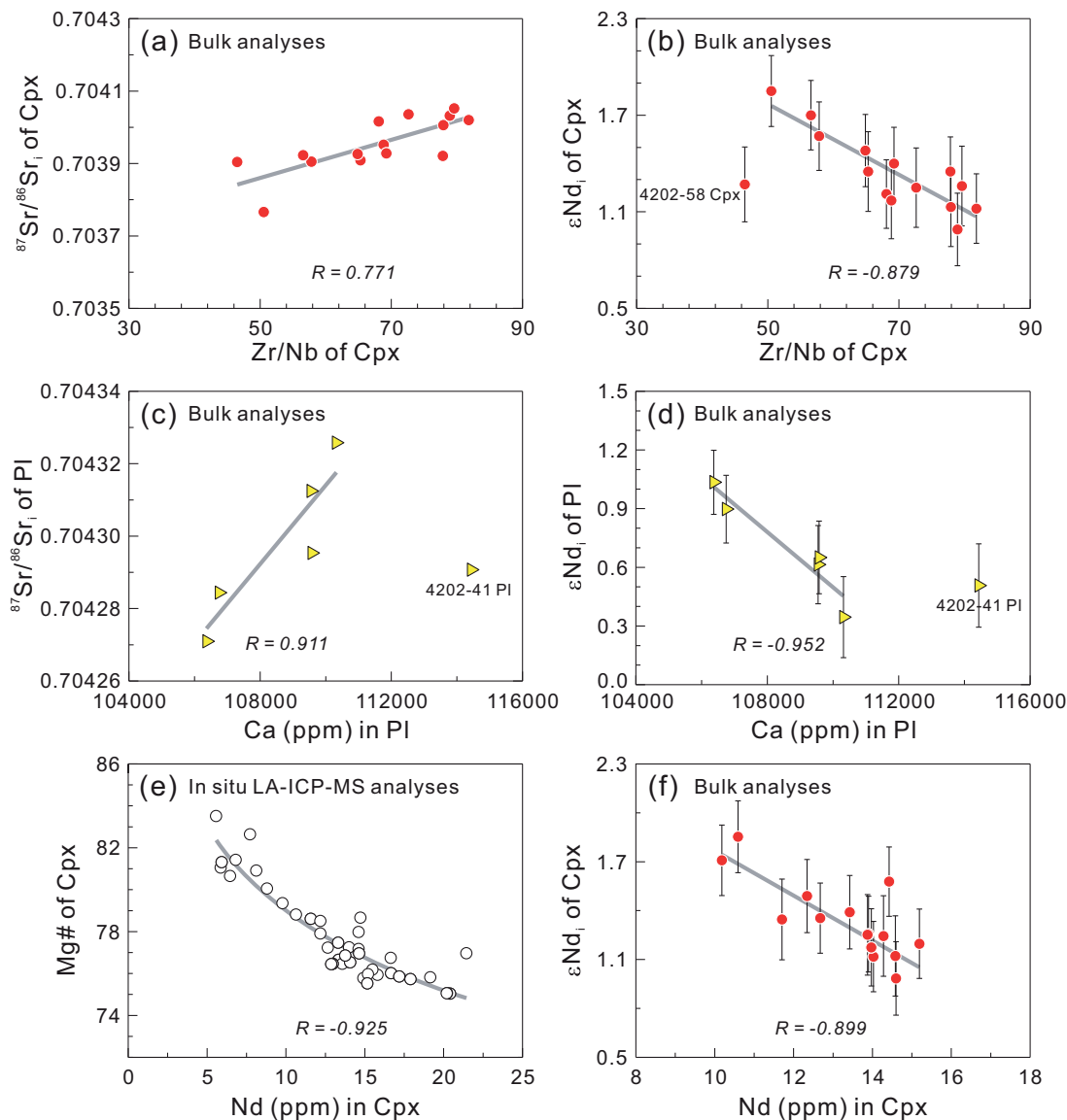


**Fig. 15.** Variation of  $^{87}\text{Sr}/^{86}\text{Sr}_i$  (a) and  $\epsilon\text{Nd}_i$  (b) vs Zr/Nb of clinopyroxene mineral separates,  $^{87}\text{Sr}/^{86}\text{Sr}_i$  (c) and  $\epsilon\text{Nd}_i$  (d) vs Ca content in plagioclase (based on total dissolution of 50 mg material), (e) Nd (*in situ* LA-ICP-MS analyses) vs Mg# of clinopyroxene and (f) Nd (bulk analyses) vs  $\epsilon\text{Nd}_i$  of clinopyroxene mineral separates. Two samples (4202-58 Cpx and 4202-41 Pl) are displaced from the trends defined by the data, which could be due to analytical problems. Error bars for  $\epsilon\text{Nd}_i$  are shown at the  $2\sigma$  level and for  $^{87}\text{Sr}/^{86}\text{Sr}_i$  the error bars are smaller than the symbols. Grey lines are regression lines with correlation coefficients (R) indicated. Cpx, clinopyroxene. Pl, plagioclase.

content in plagioclase. This suggests that the higher An plagioclase crystallized from a magma that had experienced higher degrees of contamination, inconsistent with the trend expected for an AFC process involving the Archean basement and Neoproterozoic igneous rocks as contaminants.

Assimilation of continental crust by hot, primitive mafic magmas during turbulent ascent (ATA) through conduits with very limited crystallization (Huppert & Sparks, 1985) could, however, produce trends that are opposite to those produced by an AFC process; that is, the most primitive

samples being the most contaminated (e.g. Huppert & Sparks, 1985; Kerr *et al.*, 1995). This could explain the observation made in the Xiaohaizi case that plagioclases with higher An contents have higher  $^{87}\text{Sr}/^{86}\text{Sr}_i$  and lower  $\epsilon\text{Nd}_i$ . In principle, such an ATA process could also explain the Nd–Sr isotope compositions of the clinopyroxenes. It has been suggested that ATA is mathematically equivalent to simple binary mixing between a primitive magma and the continental crust (Kerr *et al.*, 1995). In this scheme, different isotopic compositions are expected for the more primitive (more contaminated) and the more evolved

(less contaminated) samples (Merle *et al.*, 2014). However, this is not the case for the clinopyroxene separates (Fig. 15e and f). The Nd content (*in situ* LA-ICP-MS analyses) of clinopyroxene correlates negatively with Mg# (Fig. 15e), indicating that more primitive clinopyroxene compositions have lower Nd contents. Clinopyroxene separates with low Nd contents have high  $\epsilon\text{Nd}_i$  (Fig. 15f), suggesting that the more primitive clinopyroxene has a higher  $\epsilon\text{Nd}_i$  (i.e. is less contaminated). This is inconsistent with ATA predictions (Kerr *et al.*, 1995). Our favored explanation for the higher An plagioclases reflecting more contamination (Fig. 15c and d) is that the parental magma assimilated carbonate sediments with high CaO contents in addition to the Tarim igneous basement during AFC processes. In the Bachu area, the Cambrian and Ordovician strata are dominated by dolostone and limestone, respectively, and the Carboniferous–Early Permian strata contain abundant limestone (BGMRXUAR, 1993; Zhang, 2003). Moreover, industrial drilling has revealed that mafic cumulates are restricted around the Xiaohaizi syenite, indicating that the Xiaohaizi intrusion probably represents a small magma storage system. The rate of change in magma composition owing to putative *in situ* wall-rock contamination would very probably have been much quicker than in larger intrusions, having a great effect on the magma composition. Therefore, bulk assimilation of crustal carbonates will increase the CaO content of the magma, or at least compensate for the decrease in magma CaO content caused by clinopyroxene fractionation. Thus the resultant magma will crystallize higher An plagioclase.

Crustal assimilation was investigated using the approach of DePaolo (1981) for bulk assimilation with concomitant fractional crystallization (AFC). A hybrid crustal component of 30% carbonate and 70% Tarim Archean and Neoproterozoic basement was utilized as the contaminant. The Xiaohaizi dykes have higher Pb isotopic compositions than the plagioclase separates (Fig. 11c and d) and also have the lowest Sr isotope and highest Nd isotope composition among all the rocks found in the Xiaohaizi area. The Sr–Nd–Pb isotopic composition of the dykes, therefore, is a good proxy for the uncontaminated magma and is chosen as the starting isotopic composition. Because clinopyroxenes in the Xiaohaizi wehrlite intrusion and the Xiaohaizi dykes display similar trace element patterns to the Emeishan clinopyroxenes and their host high-Ti basalts, respectively, an Emeishan high-Ti picrite (EM-79; Chung & Jahn, 1995) was chosen as the starting magma composition. Figure 11a shows that the total Sr–Nd isotope dataset conforms well to an AFC model. The clinopyroxenes and plagioclases require 7–10% and 10–13% contamination, respectively. In Pb isotope space (Fig. 11c and d), calculations show that to explain the Pb isotopic variations of plagioclase, 5–14% contamination is

required. The degree of contamination calculated from the plagioclase Pb isotope compositions is more variable than that from Sr–Nd isotopes. Few Pb isotope data are available for the Tarim basement and crustal carbonates. As a consequence, the modeling for Pb isotope is less well constrained than for Sr and Nd isotopes.

It has been suggested that modeling AFC processes without considering the energy constraint is physically unrealistic (Spera & Bohrsen, 2001). As a consequence, a more consistent model for AFC (EC-AFC; Spera & Bohrsen, 2001) has been developed to constrain this parameter. In the case of the Xiaohaizi wehrlite intrusion, this model cannot be employed accurately as many of the required input data (e.g. magma liquidus temperature, country-rock temperature at the timing of magma injection) are not well constrained. However, the results of EC-AFC simulations for intrusion of basaltic magma into the upper continental crust demonstrate that the amount of assimilation calculated with EC-AFC (Bohrson & Spera, 2001) is lower than that calculated using the equations of DePaolo (1981). Therefore, our estimates of 7–10% and 10–13% contamination for clinopyroxene and plagioclase, respectively, in the Xiaohaizi wehrlite intrusion are an upper limit.

### Genetic relationships between wehrlites, dykes, syenites and quartz syenite porphyries

The Xiaohaizi intrusive complex includes wehrlites, dykes, syenites and quartz syenite porphyries. Field relationships demonstrate that the wehrlites were formed earlier than the syenites, dykes and quartz syenite porphyries. The dykes, syenites and quartz syenite porphyries have higher  $\epsilon\text{Nd}_i$  and lower  $(^{87}\text{Sr}/^{86}\text{Sr})_i$  than the wehrlites (Fig. 11a), indicating that they were derived from different magma pulses.

We suggest that the Xiaohaizi syenites and quartz syenite porphyries are formed from closed-system crystal fractionation of magmas similar to the parental magma of the dykes based on the following: (1) on various major and trace element plots they form coherent correlations (Supplementary Figs 4 and 5; Wei & Xu, 2011); (2) these rocks display similar REE and trace element patterns (Fig. 10) and have near identical Sr–Nd isotopic compositions (Fig. 11a); (3) geochemical modeling indicates that covariations of compatible (e.g. V and Ni) versus incompatible elements (e.g. Zr) can be reproduced by fractional crystallization rather than single-stage partial melting of the mafic dykes (Supplementary Fig. 5c and d). The similar trace element characteristics of the syenites and the dykes (Table 2, Fig. 10 and Supplementary Dataset 11) can be accounted for by K-feldspar accumulation in the syenites, as suggested by the moderate Eu anomalies (1.2–1.7; Wei & Xu, 2011). Accumulation of K-feldspars in the syenites



can significantly dilute certain trace elements (e.g. REE except Eu; Rollinson, 1993) that are not hosted in feldspar (Peccerillo *et al.*, 2003).

The Xiaohaizi intrusive complex might have been a long-lived, periodically refilled magma chamber with different batches of primitive magma introduced into the chamber. The cumulate wehrlites could be the products of a batch of magma that 'matured' in the chamber. After emplacement into the upper crust the magma will begin to crystallize and assimilate its wall-rocks (igneous rocks and carbonate sediments) by an AFC process. Olivine and clinopyroxene accumulated first and then plagioclase crystallized from the interstitial liquid, which was increasingly contaminated. Following deposition of the cumulate wehrlites the chamber was refilled with a fresh batch of primitive magma that evolved only through fractional crystallization forming the syenites and quartz syenite porphyries.

### Origin of high An content plagioclase

Plagioclase An content is a reliable indicator of magmatic differentiation and is frequently utilized to investigate processes involved in the formation of igneous cumulates (e.g. Humphreys, 2009; Egorova & Latypov, 2012, 2013). In layered intrusions formed from a single magma pulse the An contents of cumulus plagioclase can vary considerably; for example, 45–70 for megacyclic unit (MCU) I of the Sept Iles intrusion of Canada (Namur *et al.*, 2010), 24–70 for the Middle Zone of the Panzhihua intrusion of the Emeishan LIP (Pang *et al.*, 2009), and 33–61 for interstitial plagioclases in the clinopyroxenites of the Wajilitag layered intrusion (Cao *et al.*, 2014). The decreasing An contents reflect increasing differentiation of the melt forming the cumulus plagioclase. Additionally, plagioclase in layered intrusions in equilibrium with clinopyroxene of Mg# < 80 commonly has low An contents; for example, An < 72 for the Sept Iles layered intrusion (Namur *et al.*, 2011), An < 77 for the Hongge layered intrusion of the Emeishan LIP (Bai, 2011), An < 70 for the Panzhihua layered intrusion of the Emeishan LIP (Pang *et al.*, 2009) and An < 80 for the Bushveld Complex of South Africa (Ashwal *et al.*, 2005; Tegner *et al.*, 2006; Fig. 5f).

Plagioclase in the Xiaohaizi cumulate wehrlites displays a wide range in An content (53–86) (Supplementary Dataset 5), consistent with differentiation of the interstitial liquid. More interestingly, some of the Xiaohaizi plagioclases have unusually high An contents (up to 86). Similar high-An plagioclase (~87) is found in the middle olivine–pyroxene–plagioclase cumulate zone of the Lilloise intrusion of East Greenland (Chambers & Brown, 1995). The Lilloise intrusion has been interpreted as being formed from a hydrous alkali picritic magma (Chambers & Brown, 1995). The Xiaohaizi wehrlites display many features (e.g. cumulus mineral assemblages, clinopyroxene compositions and alkali parental magma; Fig. 4) similar

to those of the lower zone of the Lilloise intrusion. We discuss below whether H<sub>2</sub>O exerts a major control in the generation of high-An plagioclase in the Xiaohaizi wehrlite intrusion.

The formation of high-An plagioclase is dependent upon three parameters: (1) melt Ca/Na and Al/Si; (2) pressure; (3) the abundance of H<sub>2</sub>O in the magma. Melt Ca/Na and Al/Si are the major controls on the plagioclase composition: melts with high Ca/Na (and Al/Si) will crystallize plagioclase with a high An content (Elthon & Casey, 1985; Panjasawatwong *et al.*, 1995; Namur *et al.*, 2012). The parental magma of the Xiaohaizi wehrlites is an alkali basalt (Fig. 4b), compositionally similar to the crosscutting dykes. In the Xiaohaizi area the least evolved mafic dyke (W13) with a relatively high Mg# (~56) is regarded as the parental magma of the dykes and the mafic–ultramafic rocks in the Wajilitag complex (Zhang *et al.*, 2008a; Cao *et al.*, 2014). This dyke has a similar Ca/Na ratio (molar Ca/Na = 4.0) to Emeishan high-Ti melt inclusions (2.5–4.5, Kamenetsky *et al.*, 2012). In addition, the compositions of clinopyroxenes in the Xiaohaizi wehrlites bear a strong resemblance to those in the Panzhihua and Hongge layered intrusions (Pang *et al.*, 2009; Bai *et al.*, 2012). It has been widely proposed that the parental magma of the Panzhihua and Hongge layered intrusions is similar in composition to that of the Emeishan high-Ti basalts (Pang *et al.*, 2008a, 2009; Zhou *et al.*, 2008; Bai *et al.*, 2012; Song *et al.*, 2013). All these considerations lead us to suggest that the CaO content of the parental magma of the Xiaohaizi wehrlites is similar to that of the Emeishan high-Ti basalts. Melts with such Ca/Na ratios are incapable of crystallizing high-An plagioclase under relatively low pressure (<3 kbar, Pang *et al.*, 2008a; Song *et al.*, 2013) and water contents (~1.5 wt %, Pang *et al.*, 2008a). Assimilation of carbonate sediments in mafic–ultramafic intrusions is expected to increase the Ca content in the melt, thus probably resulting in crystallization of high-An plagioclase. The Panzhihua intrusion experienced 8–14% contamination by carbonate wall-rocks (marls and dolomites) (Ganino *et al.*, 2008, 2013a, 2013b). However, no plagioclase with an An content higher than 80 was observed in the Panzhihua intrusion (Pang *et al.*, 2009). As discussed above, the Xiaohaizi wehrlites experienced similar amount (<13%) of assimilation of sedimentary carbonate. Therefore, assimilation of carbonates was unlikely to be responsible for the formation of high-An content plagioclase.

Pressure also exerts a control on the anorthite content of plagioclase, with an approximate increase of ~2 mol % anorthite expected per 1 kbar drop in pressure (Panjasawatwong *et al.*, 1995). Higher H<sub>2</sub>O activity increases the equilibrium anorthite content of the melt by ~2 mol % per 1 wt % H<sub>2</sub>O (Panjasawatwong *et al.*, 1995). Modelling results for the Panzhihua intrusion show that the initial An content of plagioclase increases from 55 for

a dry magma to 73 for a magma containing 3 wt % H<sub>2</sub>O (Howarth *et al.*, 2013). Experiments have demonstrated that water lowers the liquidus temperature of silicate phases, mainly plagioclase, which saturates before Ca-rich pyroxene at low water contents and after Ca-rich pyroxene and Fe–Ti oxides at high water contents (Toplis & Carroll, 1995; Feig *et al.*, 2006, 2010; Botcharnikov *et al.*, 2008). The absence of plagioclase as a cumulus phase, therefore, indicates that the parental magma of the Xiaohaizi cumulate wehrlites was originally hydrous. Clinopyroxene in the wehrlites exhibits sporadic, patchy replacement by brown amphibole, and interstitial plagioclase and Fe–Ti oxides display reaction rims of brown amphibole. These amphiboles cannot be products of low-temperature alteration, because (1) they are closely associated with Fe–Ti oxides and occur as inclusions (Fig. 2c) and thus are isolated from any external fluid and consequent alteration; (2) the host clinopyroxenes are fairly fresh; (3) strong alteration of clinopyroxenes in some wehrlites did not give rise to amphibole (Supplementary Fig. 2d and e). Rather this could be presumably related to an aqueous vapor phase present at a later stage in the evolution of the Xiaohaizi wehrlites, supporting the suggestion of a hydrous parental magma for the wehrlites. In addition, in the Xiaohaizi wehrlites both Fe–Ti oxides and plagioclase occur as inclusions in clinopyroxene; the Fe–Ti oxides and plagioclase inclusions coexist with clinopyroxene of Mg# of up to ~84 and ~79, respectively, indicating that the crystallization of Fe–Ti oxides is earlier than that of plagioclase. This also suggests that the parental magma of the Xiaohaizi wehrlites may have been rich in H<sub>2</sub>O (Toplis & Carroll, 1995; Feig *et al.*, 2006, 2010; Botcharnikov *et al.*, 2008). H<sub>2</sub>O, therefore, might play an important role in the generation of high-An plagioclase in the Xiaohaizi wehrlite intrusion.

## CONCLUSIONS

Petrological and Sr–Nd–Pb isotopic data for selected whole-rock samples and clinopyroxene and plagioclase mineral separates allow the following conclusions to be reached regarding the genesis of the Xiaohaizi wehrlite intrusion.

- (1) The calculated liquids in equilibrium with the least evolved clinopyroxenes in the Xiaohaizi wehrlite intrusion have trace element compositions similar to those of the crosscutting dykes. However, the least contaminated dykes have apparently lower <sup>87</sup>Sr/<sup>86</sup>Sr<sub>i</sub> and higher εNd<sub>i</sub> than the intrusion. These data indicate that the Xiaohaizi wehrlite intrusion and the crosscutting dykes formed from different batches of magma derived from a similar OIB-like, enriched asthenospheric mantle source.
- (2) The cumulus clinopyroxenes and intercumulus plagioclases in the Xiaohaizi wehrlite intrusion display distinct initial Sr and Nd isotope compositions. Such isotopic disequilibrium between constituent minerals demonstrates that the plagioclase crystallized from a magma with greater extent of crustal contamination. Our Sr–Nd isotope data provide a good example of AFC processes operating during the magmatic evolution of layered mafic intrusions.
- (3) Plagioclases in the Xiaohaizi cumulate wehrlites have unusually high An contents (up to ~86), which are comparable with those in the Lilloise intrusion of East Greenland. Such high-An plagioclase cannot be formed at relatively low pressure and magma H<sub>2</sub>O contents. In considering the fractionation sequence (Ol > Cpx > Pl) in the context of experimental results, we speculate that H<sub>2</sub>O might have played an important role in the generation and evolution of the Xiaohaizi wehrlite intrusion.

## ACKNOWLEDGEMENTS

We are grateful to J. P. Guan and K. Ni for assistance in the field, X. H. Li, Q. L. Li, G. Q. Tang, Y. Liu, G. Q. Hu, X. L. Tu, C. Y. Li and L. L. Chen for technical help with diverse analyses, and Martin Menzies for help with language editing. Discussions with Professor X. L. Huang and C. Y. Wang were helpful. We are grateful to R. Merle and V. Egorova for their careful and constructive comments, which greatly improved the paper. J. Gamble is thanked for his helpful comments and editorial handling. This is contribution No IS-1987 from GIG-CAS.

## FUNDING

This work was supported by the National Basic Research Program of China (grant number 2011CB808906) and GIG-CAS 135 project (grant number Y234051001) to Y.-G.X., and the National Natural Science Foundation of China (grant number 41203009). X.W. acknowledges the support of an ARC discovery grant (DP0986542) for his visit to the University of Queensland in 2011.

## SUPPLEMENTARY DATA

Supplementary data for this paper are available at *Journal of Petrology* online.

## REFERENCES

- Aigner-Torres, M., Blundy, J., Ulmer, P. & Pettke, T. (2007). Laser ablation ICPMS study of trace element partitioning between plagioclase and basaltic melts: an experimental approach. *Contributions to Mineralogy and Petrology* **153**, 647–667.

- Anderson, J. L. & Smith, D. R. (1995). The effects of temperature and  $fO_2$  on the Al-in-hornblende barometer. *American Mineralogist* **80**, 549–559.
- Ashwal, L. D., Webb, S. J. & Knoper, M. W. (2005). Magmatic stratigraphy in the Bushveld Northern Lobe: continuous geophysical and mineralogical data from the 2950 m Bellevue drillcore. *South African Journal of Geology* **108**, 199–232.
- Bai, Z. J. (2011). Petrogenesis and Fe–Ti oxide mineralization of the mafic–ultramafic layered intrusions in the Pan-Xi area, SW China, PhD thesis, University of Chinese Academy of Sciences, 147 p. (in Chinese with English abstract).
- Bai, Z.-J., Zhong, H., Naldrett, A. J., Zhu, W.-G. & Xu, G.-W. (2012). Whole-rock and mineral composition constraints on the genesis of the giant Hongge Fe–Ti–V oxide deposit in the Emeishan Large Igneous Province, Southwest China. *Economic Geology* **107**, 507–524.
- Beattie, P. (1994). Systematics and energetics of trace-element partitioning between olivine and silicate melts: Implications for the nature of mineral/melt partitioning. *Chemical Geology* **117**, 57–71.
- BGMRXUAR. (1993). *Regional geology of the Xinjiang Uygur Autonomous Region*. Geological Publishing House, 468 p (in Chinese).
- Bindeman, I. N., Davis, A. M. & Drake, M. J. (1998). Ion microprobe study of plagioclase–basalt partition experiments at natural concentration levels of trace elements. *Geochimica et Cosmochimica Acta* **62**, 1175–1193.
- Bohrson, W. A. & Spera, F. J. (2001). Energy-constrained open-system magmatic processes II: Application of energy-constrained assimilation–fractional crystallization (EC-AFC) model to magmatic systems. *Journal of Petrology* **42**, 1019–1041.
- Botcharnikov, R. E., Almeev, R. R., Koepke, J. & Holtz, F. (2008). Phase relations and liquid lines of descent in hydrous ferrobasalt—implications for the Skaergaard intrusion and Columbia River flood basalts. *Journal of Petrology* **49**, 1687–1727.
- Cao, J., Wang, C. Y., Xing, C.-M. & Xu, Y.-G. (2014). Origin of the early Permian Wajilitag igneous complex and associated Fe–Ti oxide mineralization in the Tarim large igneous province, NW China. *Journal of Asian Earth Sciences* **84**, 51–68.
- Cao, X. F., Lu, X. B., Liu, S. T., Zhang, P., Gao, X. A., Chen, C. & Mo, Y. L. (2011). LA-ICP-MS zircon dating, geochemistry, petrogenesis and tectonic implications of the Dapingliang Neoproterozoic granites at Kuluketage block, NW China. *Precambrian Research* **186**, 205–219.
- Cawthorn, R. G. (2007). Cr and Sr: Keys to parental magmas and processes in the Bushveld Complex, South Africa. *Lithos* **95**, 381–398.
- Cawthorn, R. G., Meyer, P. S. & Kruger, F. J. (1991). Major addition of magma at the pyroxenite marker in the Western Bushveld Complex, South Africa. *Journal of Petrology* **32**, 739–763.
- Chambers, A. D. & Brown, P. E. (1995). The Lilloise intrusion, East Greenland: fractionation of a hydrous alkali picritic magma. *Journal of Petrology* **36**, 933–963.
- Chen, M. M., Tian, W., Zhang, Z. L., Pan, W. Q. & Song, Y. (2010a). Geochronology of the Permian basic–intermediate–acidic magma suite from Tarim, Northwest China and its geological implications. *Acta Petrologica Sinica* **26**, 559–572 (in Chinese with English abstract).
- Chen, Y. Q., Zhou, X. Y. & Yang, H. J. (2010b). Geochemical research and genesis of dolostones with different crystal characteristics occurring in the Upper Cambrian, central area of Tarim Basin. *Acta Sedimentologica Sinica* **28**, 209–218 (in Chinese with English abstract).
- Chung, S. L. & Jahn, B. M. (1995). Plume–lithosphere interaction in generation of the Emeishan flood basalts at the Permian–Triassic boundary. *Geology* **23**, 889–892.
- Chutas, N. I., Bates, E., Prevec, S. A., Coleman, D. S. & Boudreau, A. E. (2012). Sr and Pb isotopic disequilibrium between coexisting plagioclase and orthopyroxene in the Bushveld Complex, South Africa: microdrilling and progressive leaching evidence for sub-liquidus contamination within a crystal mush. *Contributions to Mineralogy and Petrology* **163**, 653–668.
- Class, C. & le Roex, A. P. (2008). Ce anomalies in Gough Island lavas—Trace element characteristics of a recycled sediment component. *Earth and Planetary Science Letters* **265**, 475–486.
- Collerson, K. D., Kamber, B. S. & Schoenberg, R. (2002). Applications of accurate, high-precision Pb isotope ratio measurement by multi-collector ICP-MS. *Chemical Geology* **188**, 65–83.
- Day, J. M. D., Pearson, D. G. & Hulbert, L. J. (2008). Rhenium–osmium isotope and platinum-group element constraints on the origin and evolution of the 1-27 Ga Muskox layered intrusion. *Journal of Petrology* **49**, 1255–1295.
- Deniel, C. & Pin, C. (2001). Single-stage method for the simultaneous isolation of lead and strontium from silicate samples for isotopic measurements. *Analytica Chimica Acta* **426**, 95–103.
- DePaolo, D. J. (1981). Trace element and isotopic effects of combined wallrock assimilation and fractional crystallization. *Earth and Planetary Science Letters* **53**, 189–202.
- DePaolo, D. J. & Wasserburg, G. J. (1979). Sm–Nd age of the Stillwater complex and the mantle evolution curve for neodymium. *Geochimica et Cosmochimica Acta* **43**, 999–1008.
- Dobosi, G. & Fodor, R. V. (1992). Magma fractionation, replenishment, and mixing as inferred from green-core clinopyroxenes in Pliocene basanite, southern Slovakia. *Lithos* **28**, 133–150.
- Duchesne, J. C. & Charlier, B. (2005). Geochemistry of cumulates from the Bjerkreim–Sokndal layered intrusion (S. Norway). Part I: Constraints from major elements on the mechanism of cumulate formation and on the jotunite liquid line of descent. *Lithos* **83**, 229–254.
- Egorova, V. & Latypov, R. (2012). Processes operating during the initial stage of magma chamber evolution: insights from the marginal reversal of the Imandra layered intrusion, Russia. *Journal of Petrology* **53**, 3–26.
- Egorova, V. & Latypov, R. (2013). Mafic–ultramafic sills: new insights from M- and S-shaped mineral and whole-rock compositional profiles. *Journal of Petrology* **54**, 2155–2191.
- Elthon, D. & Casey, J. F. (1985). The very depleted nature of certain primary mid-ocean ridge basalts. *Geochimica et Cosmochimica Acta* **49**, 289–298.
- Eugster, H. P. & Wones, D. R. (1962). Stability relations of the ferruginous biotite, annite. *Journal of Petrology* **3**, 82–125.
- Feig, S. T., Koepke, J. & Snow, J. E. (2006). Effect of water on tholeiitic basalt phase equilibria: an experimental study under oxidizing conditions. *Contributions to Mineralogy and Petrology* **152**, 611–638.
- Feig, S. T., Koepke, J. & Snow, J. E. (2010). Effect of oxygen fugacity and water on phase equilibria of a hydrous tholeiitic basalt. *Contributions to Mineralogy and Petrology* **160**, 551–568.
- Fourie, D. S. & Harris, C. (2011). O-isotope study of the Bushveld Complex granites and granophyres: constraints on source composition, and assimilation. *Journal of Petrology* **52**, 2221–2242.
- Frost, B. R. & Lindsley, D. H. (1991). Occurrence of iron–titanium oxides in igneous rocks. In: Rumble, D., III (ed.) *Oxide Minerals. Mineralogical Society of America, Reviews in Mineralogy* **25**, 433–468.
- Ganino, C., Arndt, N. T., Zhou, M.-F., Gaillard, F. & Chauvel, C. (2008). Interaction of magma with sedimentary wall rock and magnetite ore genesis in the Panzhihua mafic intrusion, SW China. *Mineralium Deposita* **43**, 677–694.

- Ganino, C., Arndt, N. T., Chauvel, C., Jean, A. & Athurion, C. (2013a). Melting of carbonate wall rocks and formation of the heterogeneous aureole of the Panzhihua intrusion, China. *Geoscience Frontiers* **4**, 535–546.
- Ganino, C., Harris, C., Arndt, N. T., Prevec, S. A. & Howarth, G. H. (2013b). Assimilation of carbonate country rock by the parent magma of the Panzhihua Fe–Ti–V deposit (SW China): Evidence from stable isotopes. *Geoscience Frontiers* **4**, 547–554.
- Ge, R. F., Zhu, W. B., Zheng, B. H., Wu, H. L., He, J. W. & Zhu, X. Q. (2012). Early Pan-African magmatism in the Tarim Craton: Insights from zircon U–Pb–Lu–Hf isotope and geochemistry of granitoids in the Korla area, NW China. *Precambrian Research* **212–213**, 117–138.
- Ghiorsio, M. S. & Sack, R. O. (1995). Chemical mass transfer in magmatic processes. IV. A revised and internally consistent thermodynamic model for the interpolation and extrapolation of liquid–solid equilibria in magmatic systems at elevated temperatures and pressures. *Contributions to Mineralogy and Petrology* **119**, 197–212.
- Goto, A. & Tatsumi, Y. (1996). Quantitative analysis of rock samples by an X-ray fluorescence spectrometer (II). *Rigaku Journal* **13**, 20–39.
- Haase, K. M., Hartmann, M. & Wallrabe-Adams, H.-J. (1996). The geochemistry of ashes from Vesterisbanken Seamount, Greenland Basin: Implications for the evolution of an alkaline volcano. *Journal of Volcanology and Geothermal Research* **70**, 1–19.
- Han, B. F., He, G. Q., Wang, X. C. & Guo, Z. J. (2011). Late Carboniferous collision between the Tarim and Kazakhstan–Yili terranes in the western segment of the South Tian Shan Orogen, Central Asia, and implications for the Northern Xinjiang, western China. *Earth-Science Reviews* **109**, 74–93.
- Hart, S. R. (1984). A large-scale isotope anomaly in the Southern Hemisphere mantle. *Nature* **309**, 753–757.
- Hart, S. R. & Dunn, T. (1993). Experimental cpx/melt partitioning of 24 trace elements. *Contributions to Mineralogy and Petrology* **113**, 1–8.
- Hauri, E. H., Wagner, T. P. & Grove, T. L. (1994). Experimental and natural partitioning of Th, U, Pb and other trace elements between garnet, clinopyroxene and basaltic melts. *Chemical Geology* **117**, 149–166.
- Hawkesworth, C. J., Lightfoot, P. C., Fedorenko, V. A., Blake, S., Naldrett, A. J., Doherty, W. & Gorbachev, N. S. (1995). Magma differentiation and mineralization in the Siberian continental flood basalts. *Lithos* **34**, 61–88.
- He, H., Peng, S. P. & Shao, L. Y. (2004). Trace elements and sedimentary settings of Cambrian–Ordovician carbonates in Bachu area, Tarim Basin. *Xinjiang Petroleum Geology* **25**, 631–633 (in Chinese with English abstract).
- Hofmann, A. W. (2003). Sampling mantle heterogeneity through oceanic basalts: isotopes and trace elements. In: Holland, D. D. & Turekian, K. K. (eds) *Geochemistry of the Mantle and Core: Treatise on Geochemistry*. Pergamon, pp. 61–101.
- Howarth, G. H., Prevec, S. A. & Zhou, M. F. (2013). Timing of Ti-magnetite crystallisation and silicate disequilibrium in the Panzhihua mafic layered intrusion: Implications for ore-forming processes. *Lithos* **170**, 73–89.
- Hu, A. Q., Jahn, B. M., Zhang, G. X., Chen, Y. B. & Zhang, Q. F. (2000). Crustal evolution and Phanerozoic crustal growth in northern Xinjiang: Nd isotopic evidence. Part I. Isotopic characterization of basement rocks. *Tectonophysics* **328**, 15–51.
- Humphreys, M. C. S. (2009). Chemical evolution of intercumulus liquid, as recorded in plagioclase overgrowth rims from the Skaergaard intrusion. *Journal of Petrology* **50**, 127–145.
- Huppert, H. E. & Sparks, R. S. J. (1985). Cooling and contamination of mafic and ultramafic magmas during ascent through continental crust. *Earth and Planetary Science Letters* **74**, 371–386.
- Irvine, T. N. & Baragar, W. R. A. (1971). A guide to the chemical classification of the common volcanic rocks. *Canadian Journal of Earth Sciences* **8**, 523–548.
- Jacobsen, S. B. & Wasserburg, G. J. (1980). Sm–Nd isotopic evolution of chondrites. *Earth and Planetary Science Letters* **50**, 139–155.
- Jiang, C. Y., Zhang, P. B., Lu, D. R., Bai, K. Y., Wang, Y. P., Tang, S. H., Wang, J. H. & Yang, C. (2004). Petrology, geochemistry and petrogenesis of the Kalpin basalts and their Nd, Sr and Pb isotopic compositions. *Geological Review* **50**, 492–500 (in Chinese with English abstract).
- Kamenetsky, V. S., Chung, S. L., Kamenetsky, M. B. & Kuzmin, D. V. (2012). Picrites from the Emeishan Large Igneous Province, SW China: a compositional continuum in primitive magmas and their respective mantle sources. *Journal of Petrology* **53**, 2095–2113.
- Kerr, A. C., Kempton, P. D. & Thompson, R. N. (1995). Crustal assimilation during turbulent magma ascent (ATA): new isotopic evidence from the Mull Tertiary lava succession, N. W. Scotland. *Contributions to Mineralogy and Petrology* **119**, 142–154.
- Klemme, S., Gunther, D., Hametner, K., Prowatke, S. & Zack, T. (2006). The partitioning of trace elements between ilmenite, ulvöspinel, armalcolite and silicate melts with implications for the early differentiation of the moon. *Chemical Geology* **234**, 251–263.
- Kruger, F. J., Cawthorn, R. G. & Walsh, K. L. (1987). Strontium isotopic evidence against magma addition in the Upper Zone of the Bushveld Complex. *Earth and Planetary Science Letters* **84**, 51–58.
- Le Bas, M. J., LeMaitre, R. W., Streckeis, A. & Zanettin, B. (1986). A chemical classification of volcanic rocks based on the total alkali–silica diagram. *Journal of Petrology* **27**, 745–750.
- Leeman, W. P., Ma, M. S., Murali, A. V. & Schmitt, R. A. (1978). Empirical estimation of magnetite/liquid distribution coefficients for some transition elements. *Contributions to Mineralogy and Petrology* **65**, 269–272.
- Lepage, L. D. (2003). ILMAT: an Excel worksheet for ilmenite–magnetite geothermometry and geobarometry. *Computers and Geosciences* **29**, 673–678.
- Leterrier, J., Maury, R. C., Thonon, P., Girard, D. & Marchal, M. (1982). Clinopyroxene composition as a method of identification of the magmatic affinities of paleovolcanic series. *Earth and Planetary Science Letters* **59**, 139–154.
- Li, P. C., Chen, G. H., Zeng, Q. S., Yi, J. & Hu, G. (2011a). Genesis of Lower Ordovician dolomite in Central Tarim Basin. *Acta Sedimentologica Sinica* **29**, 842–856 (in Chinese with English abstract).
- Li, Q. L., Li, X. H., Liu, Y., Tang, G. Q., Yang, J. H. & Zhu, W. G. (2010). Precise U–Pb and Pb–Pb dating of Phanerozoic baddeleyite by SIMS with oxygen flooding technique. *Journal of Analytical Atomic Spectrometry* **25**, 1107–1113.
- Li, X. H., Liu, Y., Li, Q. L., Guo, C. H. & Chamberlain, K. R. (2009). Precise determination of Phanerozoic zircon Pb/Pb age by multi-collector SIMS without external standardization. *Geochemistry, Geophysics, Geosystems* **10**, doi:10.1029/2009GC002400.
- Li, Y., Su, W., Kong, P., Qian, Y. X., Zhang, K. Y., Zhang, M. L., Chen, Y., Cai, X. Y. & You, D. H. (2007). Zircon U–Pb ages of the early Permian magmatic rocks in the Tazhong–Bachu region, Tarim basin by LA-ICP-MS. *Acta Petrologica Sinica* **23**, 1097–1107 (in Chinese with English abstract).
- Li, Y. Q., Li, Z. L., Chen, H. L., Yang, S. F. & Yu, X. (2012a). Mineral characteristics and metallogenesis of the Wajilitag layered mafic–ultramafic intrusion and associated Fe–Ti–V oxide deposit in the



- Tarim large igneous province, northwest China. *Journal of Asian Earth Sciences* **49**, 161–174.
- Li, Y. Q., Li, Z. L., Sun, Y. L., Santosh, M., Langmuir, C. H., Chen, H. L., Yang, S. F., Chen, Z. X. & Yu, X. (2012b). Platinum-group elements and geochemical characteristics of the Permian continental flood basalts in the Tarim Basin, northwest China: Implications for the evolution of the Tarim Large Igneous Province. *Chemical Geology* **328**, 278–289.
- Li, Z. L., Yang, S. F., Chen, H. L., Langmuir, C. H., Yu, X., Lin, X. B. & Li, Y. Q. (2008). Chronology and geochemistry of Taxinan basalts from the Tarim basin: evidence for Permian plume magmatism. *Acta Petrologica Sinica* **24**, 959–970 (in Chinese with English abstract).
- Li, Z. L., Chen, H. L., Song, B. A., Li, Y. Q., Yang, S. F. & Yu, X. (2011b). Temporal evolution of the Permian large igneous province in Tarim Basin in northwestern China. *Journal of Asian Earth Sciences* **42**, 917–927.
- Lightfoot, P. C., Naldrett, A. J., Gorbachev, N. S., Doherty, W. & Fedorenko, V. A. (1990). Geochemistry of the Siberian trap of the Norilsk area, USSR, with implications for the relative contributions of crust and mantle to flood-basalt magmatism. *Contributions to Mineralogy and Petrology* **104**, 631–644.
- Liu, Y., Liu, H. C. & Li, X. H. (1996). Simultaneous and precise determination of 40 trace elements in rock samples using ICP-MS. *Geochimica* **25**, 552–558 (in Chinese with English abstract).
- Long, X. P., Yuan, C., Sun, M., Zhao, G. C., Xiao, W. J., Wang, Y. J., Yang, Y. H. & Hu, A. Q. (2010). Archean crustal evolution of the northern Tarim craton, NW China: Zircon U–Pb and Hf isotopic constraints. *Precambrian Research* **180**, 272–284.
- Long, X. P., Yuan, C., Sun, M., Kröner, A., Zhao, G. C., Wilde, S. & Hu, A. Q. (2011). Reworking of the Tarim Craton by underplating of mantle plume-derived magmas: Evidence from Neoproterozoic granitoids in the Kuluketage area, NW China. *Precambrian Research* **187**, 1–14.
- Lu, S. N., Zhao, G. C., Wang, H. C. & Hao, G. J. (2008). Precambrian metamorphic basement and sedimentary cover of the North China Craton: A review. *Precambrian Research* **160**, 77–93.
- Ludwig, K. R. (2003). User's manual for Isoplot 3.00: a geochronological toolkit for Microsoft Excel. *Berkeley Geochronology Centre Special Publication* **4**.
- Maier, W. D., Arndt, N. T. & Curl, E. A. (2000). Progressive crustal contamination of the Bushveld Complex: evidence from Nd isotopic analyses of the cumulate rocks. *Contributions to Mineralogy and Petrology* **140**, 316–327.
- Mathez, E. A. & Kent, A. J. R. (2007). Variable initial Pb isotopic compositions of rocks associated with the UG2 chromitite, eastern Bushveld Complex. *Geochimica et Cosmochimica Acta* **71**, 5514–5527.
- Mathez, E. A. & Waight, T. E. (2003). Lead isotopic disequilibrium between sulfide and plagioclase in the Bushveld Complex and the chemical evolution of large layered intrusions. *Geochimica et Cosmochimica Acta* **67**, 1875–1888.
- McDonough, W. F. & Sun, S. S. (1995). The composition of the earth. *Chemical Geology* **120**, 223–253.
- Merle, R., Marzoli, A., Reisberg, L., Bertrand, H., Nemchin, A., Chiaradia, M., Callegaro, S., Jourdan, F., Bellieni, G., Kontak, D., Puffer, J. & McHone, J. G. (2014). Sr, Nd, Pb and Os isotope systematics of CAMP tholeiites from Eastern North America (ENA): evidence of a subduction-enriched mantle source. *Journal of Petrology* **55**, 133–180.
- Míková, J. & Denková, P. (2007). Modified chromatographic separation scheme for Sr and Nd isotope analysis in geological silicate samples. *Journal of Geosciences* **52**, 221–226.
- Morimoto, N., Fabries, J., Ferguson, A. K., Ginzburg, I. V., Ross, M., Seifert, F. A., Zussman, J., Aoki, K. & Gottardi, G. (1988). Nomenclature of pyroxenes. *American Mineralogist* **73**, 1123–1133.
- Naldrett, A. J., Lightfoot, P. C., Fedorenko, V., Doherty, W. & Gorbachev, N. S. (1992). Geology and geochemistry of intrusions and flood basalts of the Norilsk region, USSR, with implications for the origin of the Ni–Cu ores. *Economic Geology* **87**, 975–1004.
- Namur, O., Charlier, B., Toplis, M. J., Higgins, M. D., Liegeois, J.-P. & Vander Auwera, J. (2010). Crystallization sequence and magma chamber processes in the ferrobaltic Sept Iles layered intrusion, Canada. *Journal of Petrology* **51**, 1203–1236.
- Namur, O., Charlier, B., Pirard, C., Hermann, J., Liégeois, J.-P. & Auwera, J. V. (2011). Anorthosite formation by plagioclase flotation in ferrobaltic and implications for the lunar crust. *Geochimica et Cosmochimica Acta* **75**, 4998–5018.
- Namur, O., Charlier, B., Toplis, M. J. & Vander Auwera, J. (2012). Prediction of plagioclase–melt equilibria in anhydrous silicate melts at 1 atm. *Contributions to Mineralogy and Petrology* **163**, 133–150.
- Nebel, O., Arculus, R. J., Ivancic, T. J. & Nebel-Jacobsen, Y. J. (2013). Lu–Hf isotopic memory of plume–lithosphere interaction in the source of layered mafic intrusions, Windimurra Igneous Complex, Yilgarn Craton, Australia. *Earth and Planetary Science Letters* **380**, 151–161.
- Norman, M., Garcia, M. O. & Pietruszka, A. J. (2005). Trace-element distribution coefficients for pyroxenes, plagioclase, and olivine in evolved tholeiites from the 1955 eruption of Kilauea Volcano, Hawai'i, and petrogenesis of differentiated rift-zone lavas. *American Mineralogist* **90**, 888–899.
- O'Driscoll, B., Day, J. M. D., Daly, J. S., Walker, R. J. & McDonough, W. F. (2009). Rhenium–osmium isotopes and platinum-group elements in the Rum Layered Suite, Scotland: Implications for Cr–spinel seam formation and the composition of the Iceland mantle anomaly. *Earth and Planetary Science Letters* **286**, 41–51.
- Pang, K. N., Li, C. S., Zhou, M. F. & Ripley, E. M. (2008a). Abundant Fe–Ti oxide inclusions in olivine from the Panzhihua and Hongge layered intrusions, SW China: evidence for early saturation of Fe–Ti oxides in ferrobaltic magma. *Contributions to Mineralogy and Petrology* **156**, 307–321.
- Pang, K. N., Zhou, M. F., Lindsley, D., Zhao, D. G. & Malpas, J. (2008b). Origin of Fe–Ti oxide ores in mafic intrusions: Evidence from the Panzhihua intrusion, SW China. *Journal of Petrology* **49**, 295–313.
- Pang, K. N., Li, C. S., Zhou, M. F. & Ripley, E. M. (2009). Mineral compositional constraints on petrogenesis and oxide ore genesis of the late Permian Panzhihua layered gabbroic intrusion, SW China. *Lithos* **110**, 199–214.
- Panjasawatwong, Y., Danyushevsky, L. V., Crawford, A. J. & Harris, K. L. (1995). An experimental study of the effects of melt composition on plagioclase–melt equilibria at 5 and 10 kbar: implications for the origin of magmatic high-An plagioclase. *Contributions to Mineralogy and Petrology* **118**, 420–432.
- Peccerillo, A., Barberio, M. R., Yirgu, G., Ayalew, D., Barbieri, M. & Wu, T. W. (2003). Relationships between mafic and peralkaline silicic magmatism in continental rift settings: A petrological, geochemical and isotopic study of the Gedemsa volcano, central Ethiopian rift. *Journal of Petrology* **44**, 2003–2032.
- Pin, C. & Zalduegui, J. S. (1997). Sequential separation of light rare-earth elements, thorium and uranium by miniaturized extraction chromatography: Application to isotopic analyses of silicate rocks. *Analytica Chimica Acta* **339**, 79–89.



- Pirajno, F., Mao, J. W., Zhang, Z. C., Zhang, Z. H. & Chai, F. M. (2008). The association of mafic-ultramafic intrusions and A-type magmatism in the Tian Shan and Altay orogens, NW China: Implications for geodynamic evolution and potential for the discovery of new ore deposits. *Journal of Asian Earth Sciences* **32**, 165–183.
- Prevec, S. A., Ashwal, L. D. & Mkaza, M. S. (2005). Mineral disequilibrium in the Merensky Reef, western Bushveld Complex, South Africa: New Sm–Nd isotopic evidence. *Contributions to Mineralogy and Petrology* **149**, 306–315.
- Qi, L. & Zhou, M. F. (2008). Platinum-group elemental and Sr–Nd–Os isotopic geochemistry of Permian Emeishan flood basalts in Guizhou Province, SW China. *Chemical Geology* **248**, 83–103.
- Richardson, S. H. & Shirey, S. B. (2008). Continental mantle signature of Bushveld magmas and coeval diamonds. *Nature* **453**, 910–913.
- Roeder, P. L. & Emslie, R. F. (1970). Olivine–liquid equilibrium. *Contributions to Mineralogy and Petrology* **29**, 275–289.
- Roelofse, F. & Ashwal, L. D. (2012). The lower Main Zone in the Northern Limb of the Bushveld Complex—a >13 km thick sequence of intruded and variably contaminated crystal mushes. *Journal of Petrology* **53**, 1449–1476.
- Rollinson, H. R. (1993). *Using Geochemical Data: Evaluation, Presentation, Interpretation*. Longman.
- Salters, V. J. M. & Sachi-Kocher, A. (2010). An ancient metasomatic source for the Walvis Ridge basalts. *Chemical Geology* **273**, 151–167.
- Salters, V. J. M. & Stracke, A. (2004). Composition of the depleted mantle. *Geochemistry, Geophysics, Geosystems* **5**, doi:10.1029/2003GC000597.
- Shangguan, S. M., Tian, W., Li, X. H., Guan, P., Pan, M., Chen, M. M. & Pan, W. Q. (2011). SIMS zircon U–Pb age of a rhyolite layer from the Halahatang area, Northern Tarim, NW China: constraint on the eruption age of major pulse of Tarim flood basalt. *Acta Scientiarum Naturalium Universitatis Pekinensis* **47**, 561–564 (in Chinese with English abstract).
- Shao, L. Y., He, H., Peng, S. P. & Li, R. J. (2002). Types and origin of dolostones of the Cambrian and Ordovician of Bachu Uplift area in Tarim Basin. *Journal of Palaeogeography* **4**, 19–28 (in Chinese with English abstract).
- Song, X.-Y., Qi, H.-W., Hu, R.-Z., Chen, L.-M., Yu, S.-Y. & Zhang, J.-F. (2013). Formation of thick stratiform Fe–Ti oxide layers in layered intrusion and frequent replenishment of fractionated mafic magma: Evidence from the Panzhihua intrusion, SW China. *Geochemistry, Geophysics, Geosystems* **14**, 712–732.
- Spera, F. J. & Bohrsen, W. A. (2001). Energy-constrained open-system magmatic processes I: General model and energy-constrained assimilation and fractional crystallization (EC-AFC) formulation. *Journal of Petrology* **42**, 999–1018.
- Stacey, J. S. & Kramers, J. D. (1975). Approximation of terrestrial lead isotope evolution by a two-stage model. *Earth and Planetary Science Letters* **26**, 207–221.
- Sun, L. H., Wang, Y. J., Fan, W. M. & Zi, J. W. (2008). A further discussion of the petrogenesis and tectonic implication of the Mazhashan syenites in the Bachu area. *Journal of Jilin University (Earth Science Edition)* **38**, 8–20 (in Chinese with English abstract).
- Sun, S. S. & McDonough, W. F. (1989). Chemical and isotopic systematics of oceanic basalts: implications for mantle composition and processes. In: Saunders, A. D. & Norry, M. J. (eds) *Magmatism in the Ocean Basins*. Geological Society, London, Special Publications **42**, 313–345.
- Tanaka, T., Togashi, S., Kamioka, H., Amakawa, H., Kagami, H., Hamamoto, T., Yuhara, M., Orihashi, Y., Yoneda, S., Shimizu, H., Kunimaru, T., Takahashi, K., Yanagi, T., Nakano, T., Fujimaki, H., Shinjo, R., Asahara, Y., Tanimizu, M. & Dragusanu, C. (2000). JNdi-1: a neodymium isotopic reference in consistency with LaJolla neodymium. *Chemical Geology* **168**, 279–281.
- Tegner, C., Cawthorn, R. G. & Kruger, F. J. (2006). Cyclicity in the main and upper zones of the Bushveld Complex, South Africa: Crystallization from a zoned magma sheet. *Journal of Petrology* **47**, 2257–2279.
- Tepley, F. J. & Davidson, J. P. (2003). Mineral-scale Sr-isotope constraints on magma evolution and chamber dynamics in the Rum layered intrusion, Scotland. *Contributions to Mineralogy and Petrology* **145**, 628–641.
- Tian, W., Campbell, I. H., Allen, C. M., Guan, P., Pan, W. Q., Chen, M. M., Yu, H. J. & Zhu, W. P. (2010). The Tarim picrite-basalt–rhyolite suite, a Permian flood basalt from northwest China with contrasting rhyolites produced by fractional crystallization and anatexis. *Contributions to Mineralogy and Petrology* **160**, 407–425.
- Toplis, M. J. & Carroll, M. R. (1995). An experimental study of the influence of oxygen fugacity on Fe–Ti oxide stability, phase relations, and mineral–melt equilibria in ferro-basaltic systems. *Journal of Petrology* **36**, 1137–1170.
- Tu, X. L., Zhang, H., Deng, W. F., Ling, M. X., Liang, H. Y., Liu, Y. & Sun, W. D. (2011). Application of RESolution *in-situ* laser ablation ICP-MS in trace element analyses. *Geochimica* **40**, 83–89 (in Chinese with English abstract).
- Wass, S. Y. (1979). Multiple origins of clinopyroxenes in alkali basaltic rocks. *Lithos* **12**, 115–132.
- Wei, X. & Xu, Y. G. (2011). Petrogenesis of Xiaohaizi syenite complex from Bachu area, Tarim. *Acta Petrologica Sinica* **27**, 2984–3004 (in Chinese with English abstract).
- Wei, X. & Xu, Y. G. (2013). Petrogenesis of the mafic dykes from Bachu and implications for the magma evolution of the Tarim large igneous province, NW China. *Acta Petrologica Sinica* **29**, 3323–3335.
- Wei, X., Xu, Y. G., Feng, Y. X. & Zhao, J. X. (2014). Plume–lithosphere interaction in the generation of the Tarim large igneous province, NW China: geochronological and geochemical constraints. *American Journal of Science* **314**, 314–356.
- Wiedenbeck, M., Allé, P., Corfu, F., Griffin, W. L., Meier, M., Oberli, F., Von Quadt, A., Roddick, J. C. & Spiegel, W. (1995). Three natural zircon standards for U–Th–Pb, Lu–Hf, trace-element and REE analyses. *Geostandards Newsletter* **19**, 1–23.
- Willbold, M. & Stracke, A. (2006). Trace element composition of mantle end-members: Implications for recycling of oceanic and upper and lower continental crust. *Geochemistry, Geophysics, Geosystems* **7**, doi:10.1029/2005GC001005.
- Wilson, A. H. (2012). A chill sequence to the Bushveld Complex: insight into the first stage of emplacement and implications for the parental magmas. *Journal of Petrology* **53**, 1123–1168.
- Wood, B. J. & Blundy, J. D. (1997). A predictive model for rare earth element partitioning between clinopyroxene and anhydrous silicate melt. *Contributions to Mineralogy and Petrology* **129**, 166–181.
- Xiao, L., Xu, Y. G., Mei, H. J., Zheng, Y. F., He, B. & Pirajno, F. (2004). Distinct mantle sources of low-Ti and high-Ti basalts from the western Emeishan large igneous province, SW China: implications for plume–lithosphere interaction. *Earth and Planetary Science Letters* **228**, 525–546.
- Xu, Y. G., Chung, S. L., Jahn, B. M. & Wu, G. Y. (2001). Petrologic and geochemical constraints on the petrogenesis of Permian–Triassic Emeishan flood basalts in southwestern China. *Lithos* **58**, 145–168.
- Xu, Y. G., Wei, X., Luo, Z. Y., Liu, H. Q. & Cao, J. (2014). The Early Permian Tarim Large Igneous Province: Main characteristics and a plume incubation model. *Lithos* **204**, 20–35.

- Yang, S. F., Chen, H. L., Dong, C. W., Jia, C. Z. & Wang, Z. G. (1996). The discovery of Permian syenite inside Tarim basin and its geodynamic significance. *Geochimica* **25**, 121–128 (in Chinese with English abstract).
- Yang, S. F., Li, Z. L., Chen, H. L., Xiao, W. J., Yu, X., Lin, X. B. & Shi, X. G. (2006). Discovery of a Permian quartz syenitic porphyritic dyke from the Tarim basin and its tectonic implications. *Acta Petrologica Sinica* **22**, 1405–1412 (in Chinese with English abstract).
- Yang, S. F., Li, Z. L., Chen, H. L., Santosh, M., Dong, C. W. & Yu, X. (2007). Permian bimodal dyke of Tarim Basin, NW China: Geochemical characteristics and tectonic implications. *Gondwana Research* **12**, 113–120.
- Yang, S. H., Maier, W. D., Lahaye, Y. & O'Brien, H. (2013). Strontium isotope disequilibrium of plagioclase in the Upper Critical Zone of the Bushveld Complex: evidence for mixing of crystal slurries. *Contributions to Mineralogy and Petrology* **166**, 959–974.
- Yu, J. C., Mo, X. X., Dong, G. C., Yu, X. H., Xing, F. C., Li, Y. & Huang, X. K. (2011a). Felsic volcanic rocks from northern Tarim, NW China: Zircon U–Pb dating and geochemical characteristics. *Acta Petrologica Sinica* **27**, 2184–2194 (in Chinese with English abstract).
- Yu, X. (2009). Magma evolution and deep geological processes of early Permian Tarim large igneous province, PhD thesis, Zhejiang University (in Chinese with English abstract).
- Yu, X., Yang, S. F., Chen, H. L., Chen, Z. Q., Li, Z. L., Batt, G. E. & Li, Y. Q. (2011b). Permian flood basalts from the Tarim Basin, Northwest China: SHRIMP zircon U–Pb dating and geochemical characteristics. *Gondwana Research* **20**, 485–497.
- Zhang, C.-L. & Zou, H.-b. (2013a). Comparison between the Permian mafic dykes in Tarim and the western part of Central Asian Orogenic Belt (CAOB), NW China: Implications for two mantle domains of the Permian Tarim Large Igneous Province. *Lithos* **174**, 15–27.
- Zhang, C. L. & Zou, H. B. (2013b). Permian A-type granites in Tarim and western part of Central Asian Orogenic Belt (CAOB): Genetically related to a common Permian mantle plume? *Lithos* **172–173**, 47–60.
- Zhang, C. L., Li, X. H., Li, Z. X., Lu, S. N., Ye, H. M. & Li, H. M. (2007). Neoproterozoic ultramafic–mafic–carbonatite complex and granitoids in Quruqtagh of northeastern Tarim Block, western China: Geochronology, geochemistry and tectonic implications. *Precambrian Research* **152**, 149–169.
- Zhang, C. L., Li, X. H., Li, Z. X., Ye, H. M. & Li, C. N. (2008a). A Permian layered intrusive complex in the western Tarim Block, northwestern China: Product of a *ca.* 275-Ma mantle plume? *Journal of Geology* **116**, 269–287.
- Zhang, C. L., Xu, Y. G., Li, Z. X., Wang, H. Y. & Ye, H. M. (2010a). Diverse Permian magmatism in the Tarim Block, NW China: Genetically linked to the Permian Tarim mantle plume? *Lithos* **119**, 537–552.
- Zhang, C. L., Li, H. K., Santosh, M., Li, Z. X., Zou, H. B., Wang, H. Y. & Ye, H. M. (2012a). Precambrian evolution and cratonization of the Tarim Block, NW China: Petrology, geochemistry, Nd-isotopes and U–Pb zircon geochronology from Archaean gabbro–TTG–potassic granite suite and Paleoproterozoic metamorphic belt. *Journal of Asian Earth Sciences* **47**, 5–20.
- Zhang, D. Y., Zhou, T. F., Yuan, F., Jowitt, S. M., Fan, Y. & Liu, S. (2012b). Source, evolution and emplacement of Permian Tarim basalts: Evidence from U–Pb dating, Sr–Nd–Pb–Hf isotope systematics and whole rock geochemistry of basalts from the Keping area, Xinjiang Uygur Autonomous region, northwest China. *Journal of Asian Earth Sciences* **49**, 175–190.
- Zhang, H. A., Li, Y. J., Wu, G. Y., Su, W., Qian, Y. X., Meng, Q. L., Cai, X. Y., Han, L. J., Zhao, Y. & Liu, Y. L. (2009). Isotopic geochronology of Permian igneous rocks in the Tarim Basin. *Chinese Journal of Geology* **44**, 137–158 (in Chinese with English abstract).
- Zhang, S. B. (2003). *A Guide to the Stratigraphic Investigation on the Periphery of the Tarim Basin*. Petroleum Industry Press, 280 p (in Chinese).
- Zhang, Y. T., Liu, J. Q. & Guo, Z. F. (2010b). Permian basaltic rocks in the Tarim basin, NW China: Implications for plume–lithosphere interaction. *Gondwana Research* **18**, 596–610.
- Zhang, Z. C., Mahoney, J. J., Mao, J. W. & Wang, F. S. (2006). Geochemistry of picritic and associated basalt flows of the western Emeishan flood basalt province, China. *Journal of Petrology* **47**, 1997–2019.
- Zhang, Z. L., Qin, Q. M., Tian, W., Cao, B., Li, B. S. & Chen, M. M. (2008b). Emplacement characteristics and spatial distribution of Permian Mazhartager basic dike swarms in Bachu area, Tarim basin. *Acta Petrologica Sinica* **24**, 2273–2280 (in Chinese with English abstract).
- Zhou, M. F., Robinson, P. T., Leshner, C. M., Keays, R. R., Zhang, C. J. & Malpas, J. (2005). Geochemistry, petrogenesis and metallogenesis of the Panzhihua gabbroic layered intrusion and associated Fe–Ti–V oxide deposits, Sichuan Province, SW China. *Journal of Petrology* **46**, 2253–2280.
- Zhou, M. F., Arndt, N. T., Malpas, J., Wang, C. Y. & Kennedy, A. K. (2008). Two magma series and associated ore deposit types in the Permian Emeishan large igneous province, SW China. *Lithos* **103**, 352–368.
- Zhou, M. F., Zhao, J. H., Jiang, C. Y., Gao, J. F., Wang, W. & Yang, S. H. (2009). OIB-like, heterogeneous mantle sources of Permian basaltic magmatism in the western Tarim Basin, NW China: Implications for a possible Permian large igneous province. *Lithos* **113**, 583–594.
- Zhu, R. K., Luo, P. & Luo, Z. (2002). The isotope geochemistry characteristics of carbonate rocks in Carboniferous in Tarim Basin. *Xinjiang Petroleum Geology* **23**, 382–384 (in Chinese with English abstract).
- Zhu, W. B., Zheng, B. H., Shu, L. S., Ma, D. S., Wu, H. L., Li, Y. X., Huang, W. T. & Yu, J. J. (2011). Neoproterozoic tectonic evolution of the Precambrian Aksu blueschist terrane, northwestern Tarim, China: Insights from LA-ICP-MS zircon U–Pb ages and geochemical data. *Precambrian Research* **185**, 215–230.
- Zindler, A. & Hart, S. (1986). Chemical geodynamics. *Annual Review of Earth and Planetary Sciences* **14**, 493–571.